

# Micro-CT Characterization of the Chang'e-5 Lunar Regolith Samples



### Key Points:

- The largest image data set of lunar regolith particles was created by X-ray micro-computed tomography and machine learning-based processing
- Three-dimensional density distribution obtained through X-ray micro-computed tomography enables particle-scale mineral identification
- Chang'e-5 lunar regolith grains have a lower mean aspect ratio than the Apollo 11, 16 and Luna 16, 20 and 24 samples

### Supporting Information:

Supporting Information may be found in the online version of this article.

### Correspondence to:

Q. Zhao,  
[qi.qz.zhao@polyu.edu.hk](mailto:qi.qz.zhao@polyu.edu.hk)

### Citation:

Wu, H., Zou, Y., Zhang, C., Yang, W., Wu, B., Yung, K.-L., & Zhao, Q. (2025). Micro-CT characterization of the Chang'e-5 lunar regolith samples. *Journal of Geophysical Research: Planets*, 130, e2024JE008787. <https://doi.org/10.1029/2024JE008787>

Received 11 OCT 2024






Accepted 28 JAN 2025

### Author Contributions:

**Conceptualization:** Huanyu Wu, Yuan Zou, Chi Zhang, Wei Yang, Qi Zhao  
**Data curation:** Chi Zhang, Qi Zhao  
**Formal analysis:** Huanyu Wu, Chi Zhang, Wei Yang  
**Funding acquisition:** Wei Yang, Bo Wu, Kai-Leung Yung, Qi Zhao  
**Investigation:** Huanyu Wu, Yuan Zou, Qi Zhao  
**Methodology:** Huanyu Wu, Yuan Zou, Chi Zhang, Wei Yang, Qi Zhao  
**Project administration:** Bo Wu, Kai-Leung Yung, Qi Zhao  
**Resources:** Qi Zhao  
**Supervision:** Chi Zhang, Wei Yang, Bo Wu, Kai-Leung Yung, Qi Zhao

© 2025 The Author(s).

This is an open access article under the terms of the [Creative Commons Attribution-NonCommercial License](#), which permits use, distribution and reproduction in any medium, provided the original work is properly cited and is not used for commercial purposes.

Huanyu Wu<sup>1,2</sup> , Yuan Zou<sup>1,2</sup>, Chi Zhang<sup>3</sup> , Wei Yang<sup>3</sup> , Bo Wu<sup>2,4</sup> , Kai-Leung Yung<sup>2,5</sup>, and Qi Zhao<sup>1,2</sup> 

<sup>1</sup>Department of Civil and Environmental Engineering, The Hong Kong Polytechnic University, Hong Kong, China,

<sup>2</sup>Research Centre for Deep Space Explorations, The Hong Kong Polytechnic University, Hong Kong, China, <sup>3</sup>Key Laboratory of Earth and Planetary Physics, Institute of Geology and Geophysics, Chinese Academy of Sciences, Beijing, China, <sup>4</sup>Department of Land Surveying and Geo-Informatics, The Hong Kong Polytechnic University, Hong Kong, China,

<sup>5</sup>Department of Industrial and Systems Engineering, The Hong Kong Polytechnic University, Hong Kong, China

**Abstract** Chang'e-5 (CE-5) lunar regolith samples were scanned using X-ray micro-computed tomography (micro-CT), and over 0.7 million particles were extracted from the images through machine learning-based segmentation. This is the largest three-dimensional (3D) image data set on lunar regolith particles to date, offering a unique opportunity to study the key characteristics of the lunar regolith. The image intensity was correlated with mineral density, allowing for the assessment of the bulk density (1.58 g/cm<sup>3</sup>), true density (3.17 g/cm<sup>3</sup>), and mineralogy of the lunar regolith. Glass and plagioclase contributed 45.6 wt.% of the samples, while pyroxene and olivine made up 49.7 wt.%, and ilmenite accounted for 4.7 wt.%. The median grain size of CE-5 was 57.5 μm, smaller than the Apollo 11, 16 and Luna 16, 20 and 24 samples. Spherical harmonic (SH) analysis and aspect ratio (AR) measurement revealed that the CE-5 lunar regolith particles have more complex shapes than two common terrestrial soils and exhibit less spherical shapes than Apollo 11, 16 and Luna 16, 20 and 24 samples. We recommend using size and shape characteristics cautiously when inferring the lunar regolith maturity because the intrinsic crystal size of the protolith and complex lunar surface weathering can cause significant size and shape variations. Additionally, characterizing particle shapes requires a large sample size (>1,000) to prevent skewed results from outliers. Our non-destructive examination method offers a novel and appealing approach for analyzing critical physical, mineralogical, and morphological properties of million-scale extraterrestrial soil particles, paving the way for future deep space explorations.

**Plain Language Summary** Characterizing the lunar regolith is crucial for understanding the geological history of the Moon and future resource utilization on the Moon. By combining X-ray micro-computed tomography and advanced machine learning-based image processing techniques, we were able to extract the digital volumes of more than 700,000 lunar regolith particles from the Chang'e-5 lunar regolith samples, which is the largest three-dimensional image data set on lunar regolith particles so far. This unique data set allows the non-destructive and more reliable evaluation of the particle size distribution, mineralogy and particle shape characteristics of the Chang'e-5 lunar regolith samples. We found that the Chang'e-5 lunar regolith particles exhibit more complex shapes than typical terrestrial soils and are less spherical compared to the Apollo 11, 16 and Luna 16, 20, and 24 samples. This study not only expanded our knowledge of the lunar regolith by obtaining a more comprehensive data set but also introduced a non-destructive workflow for studying extraterrestrial geomaterials, which will be beneficial for future deep space explorations.

## 1. Introduction

Lunar exploration has become a global focal point in the field of deep space exploration. Numerous countries and private entities are investing heavily in related technologies and missions. Notable examples include NASA's Artemis program (Smith et al., 2020) and China National Space Administration's Chang'e (CE) Project (C. Li et al., 2019). These exploration programs are driven by the desire to promote in situ resource utilization and assess the feasibility of human habitation on the Moon.

On 1 December 2020, China's Chang'e-5 (CE-5) probe landed on a flat area at 43.06°N, 51.92°W in Northern Oceanus Procellarum (Wu et al., 2018). On 17 December 2020, 1,731 g of lunar regolith samples, which included 1,500 g collected by the lunar surface sampling and packing system developed by the co-author Professor K. L. Yung's team, were brought back to Earth. The landing site is one of the youngest mare basalts on the Moon with an

**Validation:** Huanyu Wu, Chi Zhang, Wei Yang  
**Visualization:** Huanyu Wu, Yuan Zou  
**Writing – original draft:** Huanyu Wu, Qi Zhao  
**Writing – review & editing:** Huanyu Wu, Chi Zhang, Wei Yang, Bo Wu, Kai-Leung Yung, Qi Zhao

estimated age of approximately 2 billion years (Morota et al., 2011; Tian et al., 2021), which is rather away from the previous nine sampling sites accomplished by NASA's Apollo missions and the USSR's Lunar missions, making the CE-5 lunar samples unique in many aspects including their chemical composition and weathering history (C. Li et al., 2022; Lu et al., 2023; Qian et al., 2020; Tian et al., 2021).

Lunar regolith refers to the fine-grained layer on the Moon that is primarily formed by constant meteorite impacts (M. Zhang et al., 2023). Examination of lunar regolith samples could provide valuable insights into various aspects of the Moon's geological history, including the composition and structure of the lunar mantle (Longhi, 1992; Wiczorek, 2006), mare volcanism (Borg et al., 2011; Snape et al., 2019; Tian et al., 2021), and surface processes such as space weathering (Gu et al., 2022; Thompson et al., 2016). Additionally, lunar regolith plays a vital role in lunar base construction and in situ resource utilization, which not only acts as a natural foundation soil on the Moon (Carrier III et al., 1972; Costes et al., 1971; Perkins & Madson, 1996), but also has the potential to be used as a construction material for habitats, roads, landing pads, and other infrastructure (Ellery, 2022). Therefore, understanding its physical properties is essential for in situ resource utilization. Recent studies on lunar regolith, specifically the analysis of CE-5 lunar samples, have significantly advanced our understanding of its properties (Chang et al., 2023; Y. Chen et al., 2023; C. Li et al., 2022; Wu et al., 2024; Xian et al., 2023; W. Yang et al., 2022; Y. Yang et al., 2022; Yao et al., 2022; H. Zhang et al., 2022). The CE-5 samples have been proven to primarily consist of basalt and mineral fragments, impact melt breccia, agglutinates, and glasses (Y. Chen et al., 2023; Zong et al., 2022). Extensive measurements have been conducted on CE-5 samples to evaluate its physical properties including size distribution, density and specific surface area (C. Li et al., 2022; H. Zhang et al., 2022). The particle shape characteristics of lunar regolith are another important physical attribute that not only directly determines its mechanical behavior (Cho et al., 2006; Rousé et al., 2008) but also records the long-term space weathering (Tsuchiyama et al., 2022; Weber et al., 2020) and solar wind irradiation (Lacznia et al., 2021).

X-ray micro-computed tomography (micro-CT), as a widely used non-destructive testing approach (Y. Chen et al., 2021; Lei et al., 2018; Zhao et al., 2020), has been employed to conduct grain-scale observations of lunar regolith samples. Matsushima et al. (2008) and Katagiri et al. (2015) studied tens of Apollo 16 lunar regolith particles by micro-CT and established a particle flow model based on the real particle shapes. Chiaramonti et al. (2017) examined the full 3D shapes of Apollo regolith particles using micro-CT and described the particles with spherical harmonic (SH) analysis. Nie et al. (2023) employed micro-CT to quantify the shape characteristics of 224 CE-5 lunar regolith particles and predicted the residual friction angle of lunar regolith. However, it is important to acknowledge that a limited number of particles may not sufficiently represent the diverse characteristics of the lunar regolith and potentially lead to skewed or incomplete findings. Although dynamic image analysis (Deitrick & Cannon, 2022; Wilkerson et al., 2024) and laser diffraction (H. Zhang et al., 2022) have demonstrated the ability to analyze the two-dimensional shape parameters of thousands of lunar regolith particles, these methods still cannot precisely reconstruct the three-dimensional (3D) surface geometry and internal structures of those particles.

In this study, we utilized X-ray micro-CT to examine the CE-5 lunar regolith samples. The grayscale micro-CT images were processed using machine learning-based segmentation methods, enabling the characterization of more than 0.7 million lunar regolith particles. Furthermore, the physical, morphological, and mineralogical properties of the regolith particles were quantitatively assessed, including particle size distribution, density, mineral content and particle shape characteristics.

## 2. Materials and Methods

### 2.1. Chang'e-5 Lunar Regolith Samples and Micro-CT Imaging

The lunar regolith samples we examined in this study are CE5C0100YJFM00103 (Figure 1a). Approximately 80 mg sample was enclosed in a long tube with an inner diameter of 2 mm (Figure 1b). A FEI HeliScan micro-CT was used to scan a 2 mm high region of interest within the tube with a spatial resolution of 0.99  $\mu\text{m}$ . The voltage for the micro-CT scan is 80 kV and the current is 100  $\mu\text{A}$ . Exposure time is 3.3 s for each frame and 8 frames were averaged for each two-dimensional (2D) radiograph, and the whole scan took approximately 30 hr for 3,060 radiographs from different angles. A 2-mm aluminum X-ray beam filter was used to reduce beam hardening artifacts. This non-destructive testing method maximized the utilization of the lunar regolith sample while minimizing any disturbance to its integrity. The 2D micro-CT radiographs were then reconstructed into a 3D

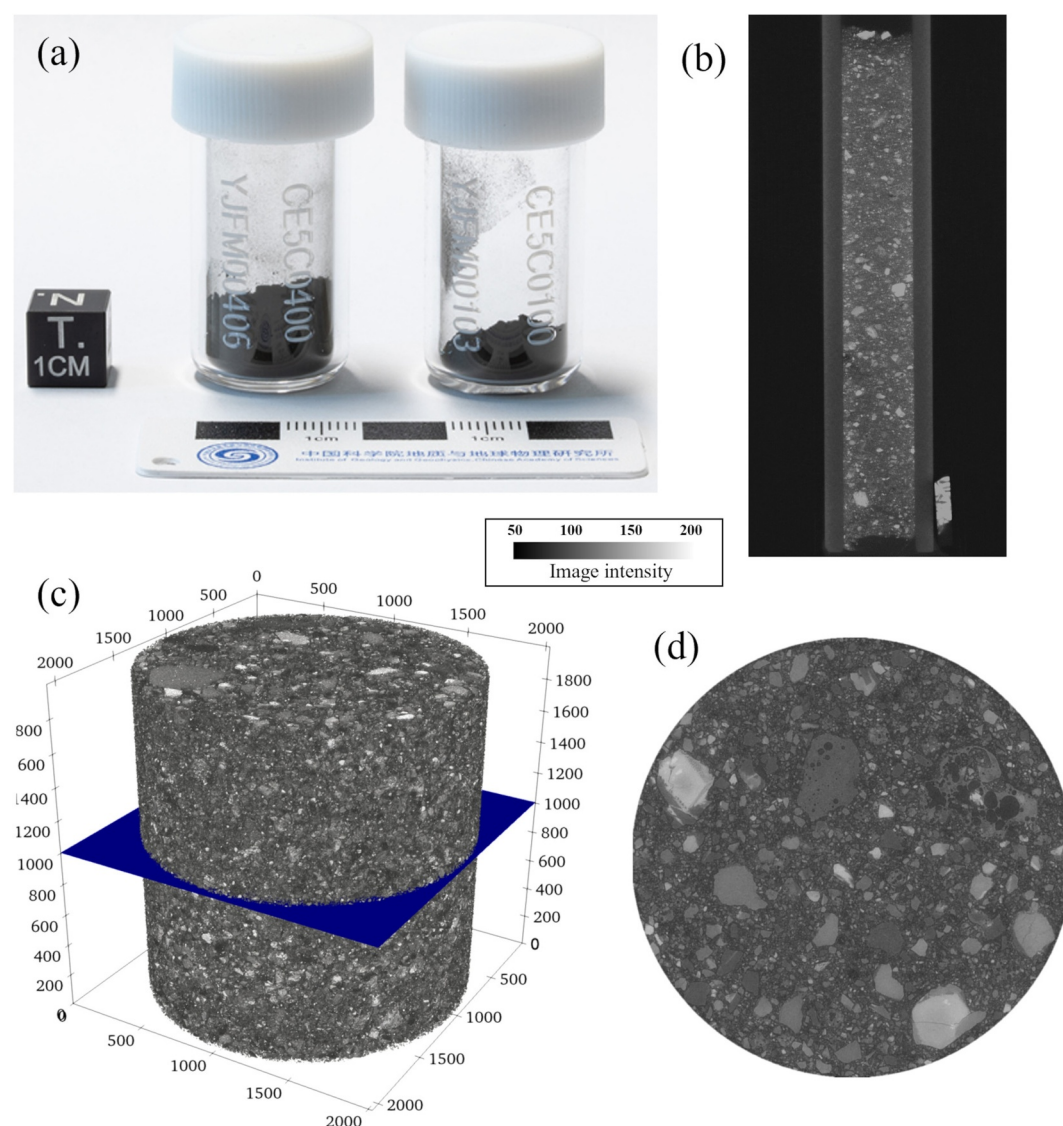


**Figure 1.** The CE-5 lunar regolith samples and micro-CT scans. (a) Lunar regolith samples CE5C0100YJFM00103 and CE5C0400YJFM00406, and the micro-CT scan data of the former is examined in this study. (b) A 2D scan at a resolution of 2.20  $\mu\text{m}$  of the tube as an overview of the sample. (c) Reconstructed grayscale volume of the sample. (d) An example horizontal slice of the sample corresponding to the middle plane in panel (c).

digital volume representing the 6.28 mm<sup>3</sup> lunar regolith by FEI Heliscan Micro-CT proprietary reconstruction software (Figures 1c and 1d) with the following settings: automatic beam hardening correction, an automatic ring artifact reduction, and a manual scan optimization that compensates for small drifts of the specimen during the scan and accurately locates the center of reconstruction. The 16-bit raw reconstructed grayscale images were converted to 8-bit, which preserves sufficient information for further analysis and reduces the memory requirement for image segmentation.

## 2.2. Machine Learning-Based Image Segmentation

Accurate segmentation of the lunar regolith particles is crucial for extracting information from the micro-CT images. Traditional methods could segment raw images into different components, such as simple thresholding (Otsu, 1979) and marker-controlled watershed algorithms (Meyer & Beucher, 1990). However, these methods may encounter challenges due to the complexity of mineral composition and intricate surface



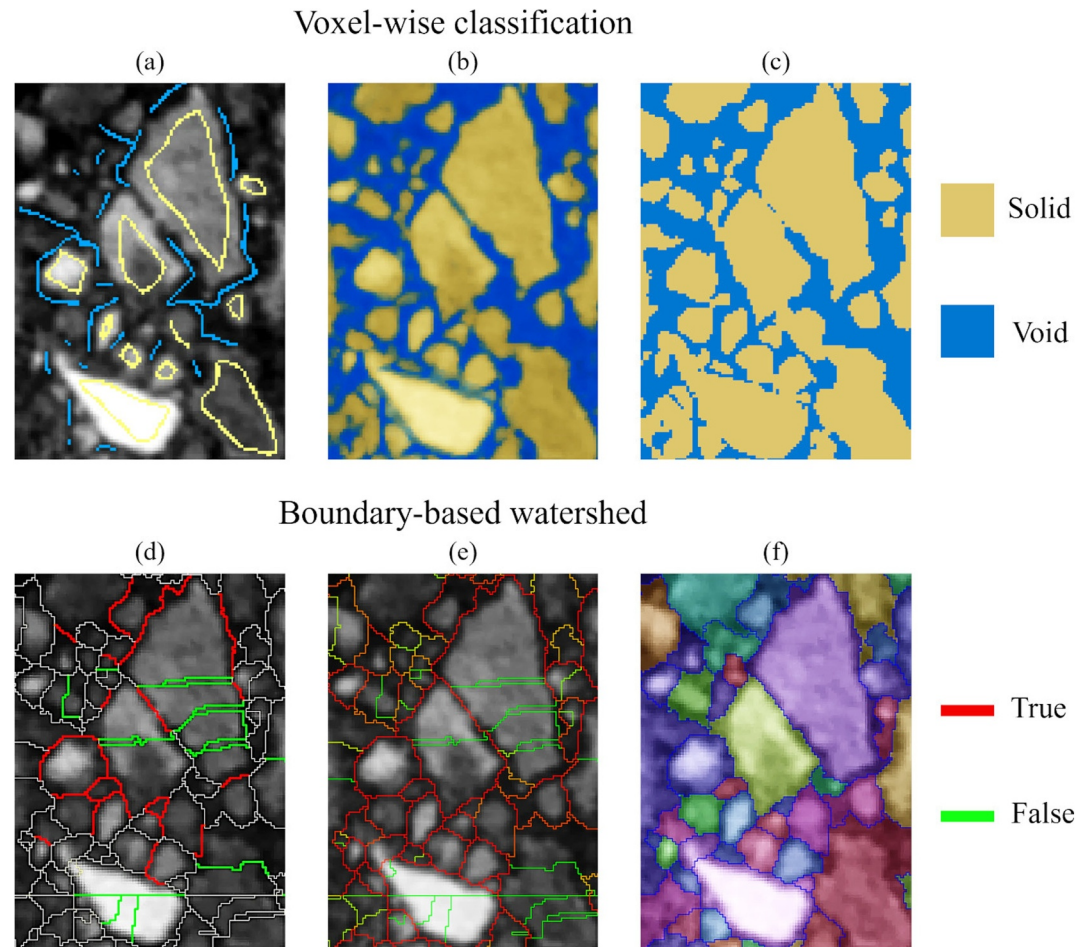


**Figure 2.** Examples of voxel-wise classification and boundary-based watershed. (a) Manually annotated micro-CT slice. (b) Probability map of voxel classification. (c) Voxel-wise classification results. (d) Predicted boundaries based on distance transform and annotations on good or bad boundaries. (e) Probability map of particle boundaries. (f) Boundary-based watershed segmentation results.

morphologies of lunar regolith particles, leading to both over-segmentation and under-segmentation. We employed a machine learning-based segmentation method to address this problem. There are two main steps involved in the 3D segmentation of lunar regolith particles: a primary voxel-wise classification that identifies different phases in the images, including solids and voids, and a secondary segmentation that isolates the individual particles based on boundaries.

The random forest algorithm presents several advantages for image segmentation applications (Breiman, 2001; Shotton et al., 2008). It is effective in managing high-dimensional data and demonstrates robustness to noise and outliers. By evaluating feature importance, this method facilitates the selection of the most relevant features. Additionally, random forest reduces overfitting and manages complex boundaries with precision. Its computational efficiency is advantageous for large data sets, and its ability to integrate diverse information types, including shape and texture, makes it particularly suitable for processing 3D micro-CT scans of lunar regolith samples.

A voxel-wise random forest classifier was employed to segment the volume data into solids (i.e., distinguishable particles with sizes larger than micro-CT resolution) and voids, considering multiple features, including intensity, boundaries and texture (Sommer et al., 2011). Arbitrarily chosen voxels were manually labeled in 2D slices according to their phase-contrast features, serving as the training set to train the random forest classifier (Figure 2a). The classifier was able to estimate the probability that a voxel belongs to each semantic class (Figure 2b). Then, a probability threshold was applied to the entire 3D volume to generate voxel-wise

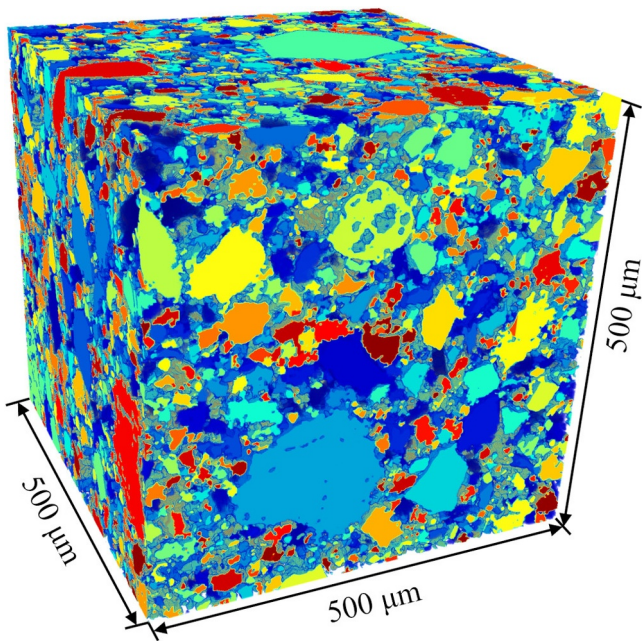


**Figure 3.** An example of the 3D segmentation. The region (500  $\mu\text{m}$   $\times$  500  $\mu\text{m}$   $\times$  500  $\mu\text{m}$ ) is cropped from the entire volume with randomly assigned pseudo-color labels for visualization.

classification results (Figure 2c). To ensure optimal accuracy, the model was iteratively updated by adding more voxel labels until satisfactory segmentation was achieved throughout the volume.

The primary segmentation could distinguish between different phases. However, the boundaries among particles typically appear to be classified as the solid phase due to the partial volume effect that is related to the limited resolution. Thus, a boundary-based watershed algorithm (Andres et al., 2011) was used to further segment the contacting assembly into isolated particles. The potential 3D boundaries (gray edges in Figure 2d) were generated by the watershed algorithm based on the distance transform. The minimum number of voxels in an isolated region is set to 10, which is the cutoff volume for particles. By training the random forest classifier using manually annotated true boundaries (in red) and false boundaries (in green) (Figure 2d), a boundary probability map (Figure 2e) was generated. The packed lunar regolith particles could be separated into distinct 3D regions with labels by applying a probability threshold (Figures 2 & 3). With this two-step image processing, the lunar regolith particles could be segmented from micro-CT images, allowing the creation of a comprehensive data set containing massive information.

### 2.3. Density Calibration

Prior studies have measured the bulk density and true density of CE-5 lunar regolith samples through the helium displacement method (C. Li et al., 2022).

However, a significant gap remains regarding the spatial density distribution within lunar regolith particles. Micro-CT imaging has emerged to interpret the density distribution within scanned samples by utilizing the correlation between grayscale image intensities and material densities (Humbert et al., 2016; Sudhyadhom, 2020). Voxel intensities of 3D micro-CT scans reflect the degree of X-ray attenuation, which is affected by several factors including the X-ray energy spectrum, scan parameters, and material properties. However, it is important to note that the primary influence on voxel intensities should be the material properties alone when using the same micro-CT machine and conducting a single scan. The voxel intensity is directly proportional to the linear attenuation coefficient  $\mu$  of the material in the corresponding spatial range, which is a product of the mass attenuation coefficient  $\mu_m$  and the material density  $\rho$ :

$$\mu = \rho \times \mu_m, \quad (1)$$

where the mass attenuation coefficient  $\mu_m$  influenced by the photoelectric effect and Compton scattering, both of which are controlled by multiple variables such as atomic number and photon energy:

$$\mu_m = \tau + \sigma \approx \alpha Z^{4.5} E^{-3} + \beta Z E^{-1}, \quad (2)$$

where  $Z$  is atomic number,  $E$  is photon energy, and  $\alpha, \beta$  are two constants. The equations above demonstrate a monotonic nonlinear relationship between voxel intensities and material densities, which illustrates that dense materials could attenuate more X-rays and result in higher voxel intensities. Therefore, it is appropriate to inversely estimate the spatial density distribution of the lunar regolith samples by means of X-ray micro-CT imaging.

To quantitatively correlate voxel intensities and material densities, several phases including air and crystallized minerals with known densities were selected as references for the calibration. The voxel intensities of multiple regions that represent distinct phases in the micro-CT images were sampled and their average values were calculated to serve as the representative intensities for distinct phases (Table S1 in Supporting Information S1). These regions were carefully confirmed to be free from artifacts or other distortions that may introduce inaccuracies (Figure 4a). By performing polynomial interpolation between discrete data points of average voxel

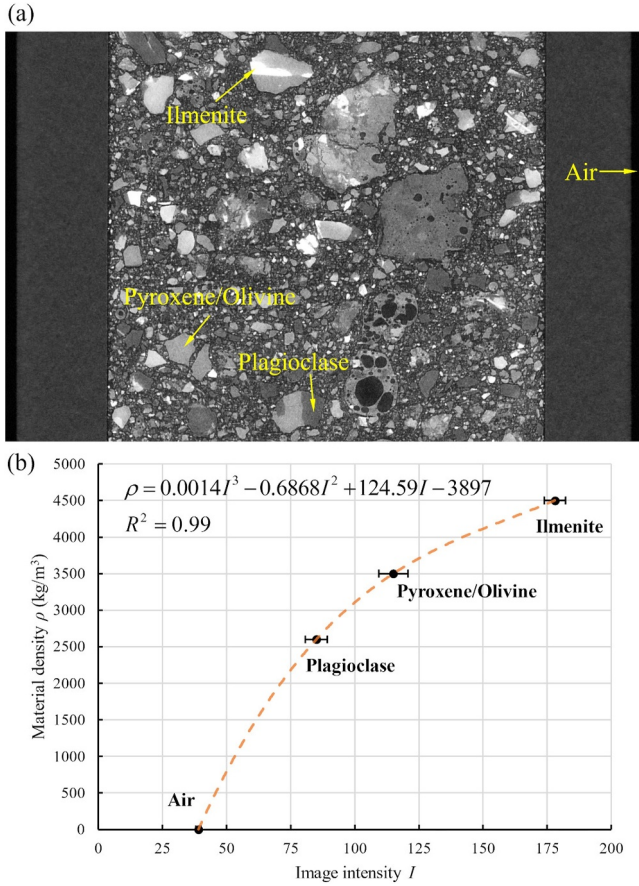


**Figure 4.** Calibration of material density based on micro-CT image intensities. (a) Phase mapping in a micro-CT slice. Four types of materials were distinguished based on phase-contrast features. (b) Fitted calibration curve of material densities and voxel intensities. Error bars show the standard deviation of the voxel intensities from sampled referencing regions.

intensities from these referencing regions and their densities, the non-linear relationship was established (Figure 4b):

$$\rho = 0.0014I^3 - 0.6868I^2 + 124.59I - 3897, \quad (3)$$

where  $\rho$  is the estimated material density,  $I$  is the intensity of the corresponding voxel in micro-CT images.

Equation 3 was then applied to convert voxel intensities into material densities, providing a spatial density distribution throughout the entire reconstructed volume, thus enabling density assessment and mineral identification within the scanned region.

#### 2.4. Quantification of Particle Shape Characteristics

The shape characteristics of lunar regolith particles are crucial for understanding the geological processes that have shaped the Moon's surface. Furthermore, it is essential to characterize and quantify the shape parameters of lunar regolith particles in order to predict their behavior in engineering applications, such as serving as foundation soils capable of bearing building loads and as potential materials for lunar base construction.

Lunar regolith particles acquire their irregular shapes as a result of constant bombardment by meteoroids and micrometeoroids during long-term space weathering (M. Zhang et al., 2023). These particles could be found in various forms, such as angular fragments, elongated shards, or agglutinates. In contrast to terrestrial soils, which tend to have round shapes, the lunar regolith particles retain their sharp edges and angular characteristics since weathering and erosion processes on the Earth are absent on the Moon.

The SH analysis is used to describe and measure the multiscale shape characteristics of particles (Y. Chen et al., 2021; Garboczi, 2002; Shen et al., 2009; Wei, Wang, Nie, & Zhou, 2018; Wei, Wang, & Zhao, 2018; Zhou et al., 2015). SH functions can be employed to represent the surfaces of particles obtained from micro-CT images:

$$r(\theta, \varphi) = \sum_{n=0}^{\infty} \sum_{m=-n}^n c_n^m Y_n^m(\theta, \varphi), \quad (4)$$

$$Y_n^m(\theta, \varphi) = \sqrt{\frac{(2n+1)(n-m)!}{4\pi(n+m)!}} P_n^m(\cos \theta) e^{im\varphi}, \quad (5)$$

where  $r(\theta, \varphi) = \sqrt{\sum_{x,y,z} (\kappa - \kappa_0)^2}$  is the polar radius from particle centroid with spherical coordinates  $\theta \in [0, \pi]$  and  $\varphi \in [0, 2\pi]$ .  $n$  is the SH degree and  $m$  is the order and  $c_n^m$  is the corresponding SH coefficient.  $P_n^m(\cos \theta)$  denotes the Legendre function of SH degree  $n$  and order  $m$ , which could be expressed by Rodrigues's formula:

$$P_n^m(x) = (1-x^2)^{|m|/2} \cdot \frac{d^{|m|}}{dx^{|m|}} \left[ \frac{1}{2^n n!} \cdot \frac{d^n}{dx^n} (x^2-1)^n \right], \quad (6)$$

By inputting the polar coordinates matrix of the discrete points on the particle surface into Equation 4, the spherical coefficients  $c_n^m$  could be obtained by solving the linear equation system using the standard least squares estimation method. The modulus of  $c_n^m$  at different spherical harmonics degree  $n$  can be calculated as follows:

$$L_n = \sqrt{\sum_{m=-n}^n \|c_n^m\|^2}. \quad (7)$$



The spherical harmonics describe the morphological features of the particle shape at different scales. A higher SH degree  $n$  allows for more detailed characterization and a more accurate reconstruction of the particle surface geometry. In this study, we adopted a maximum SH degree of 25 to analyze the multi-scale shape features of lunar regolith particles. The SH coefficients  $L_0$  represents the particle volume and  $L_1$  does not affect the particle morphology,  $L_2$  to  $L_4$  reflect the general shape,  $L_5$  to  $L_8$  depict the local roundness, while  $L_9$  and above capture the surface texture at a fine-scale level. To quantify the morphological complexity at different SH degrees, the SH descriptors  $D_n$  are proposed as follows:

$$D_n = \frac{L_n}{L_0}, (n = 2, 3, 4), \quad (8)$$

where all the  $L_n$  were divided by  $L_0$  to remove the effect of particle volume. Furthermore,  $L_1$  was not taken into consideration because it does not influence the reconstructed morphology of the particle using spherical harmonics.

Generally, the exponential relation between the SH descriptor  $D_n$  and the SH degree  $n$  can be expressed by:

$$D_n \propto n^\beta, \quad (9)$$

where  $\beta$  is the slope of the fitted line for  $\log(D_n)$  versus  $\log(n)$ . Equation 9 reflects the self-similarity of the particle shape, which can be quantified by the fractal dimension  $FD$  (Xie, 2020).  $FD$  is positively correlated with the complexity, roughness, or irregularity of the surface geometry. It could be calculated by the following expression (Russ, 2013; Wei, Wang, Nie, & Zhou, 2018; Wei, Wang, & Zhao, 2018):

$$FD = \frac{6 + \beta}{2}. \quad (10)$$

Form factors are also extensively used to quantify the overall shape characteristics of terrestrial and non-terrestrial bodies (Deitrick & Cannon, 2022; Nie et al., 2023; Zhao & Wang, 2015; Zhu & Zhao, 2021). The most widely used form factors include elongation index ( $EI$ ), flatness index ( $FI$ ) and aspect ratio ( $AR$ ) which are denoted as:

$$EI = \frac{I}{L}, \quad (11)$$

$$FI = \frac{S}{I}, \quad (12)$$

$$AR = \frac{S}{L}, \quad (13)$$

where  $L$ ,  $I$  and  $S$  are the largest, intermediate and shortest dimensions of particles obtained from a bounding box estimation, which is dependent on the order of measurement (Fujiwara et al., 1978; Katagiri et al., 2015; Michikami et al., 2018; Tsuchiyama et al., 2022). To facilitate the comparison with previous measurements, the bottom-up method (La Spina & Paolicchi, 1996) is adopted to measure the three dimensions in the order of  $S$ ,  $I$  and  $L$ , which is consistent with Tsuchiyama et al. (2022). According to the classification criteria of Zingg (1935), particles become more elongated as  $EI$  decreases and more platy as  $FI$  decreases. Conversely, as  $AR$  increases, particles become more spherical (Figure 12).

### 3. Results

#### 3.1. Reconstruction and Segmentation of Micro-CT Images

The digital volume of interest is composed of 2,000 slices of  $2025 \times 2070$  grayscale images, discretizing the samples into approximately 8,383 million voxels. With the application of machine learning-based image processing methods, the labeled grayscale volume of 710,226 lunar regolith particles was obtained (Figure 5), allowing for the observation and characterization of the individual particle structure. The segmentation results demonstrate the effectiveness of the proposed methods in accurately separating packed lunar regolith particles in

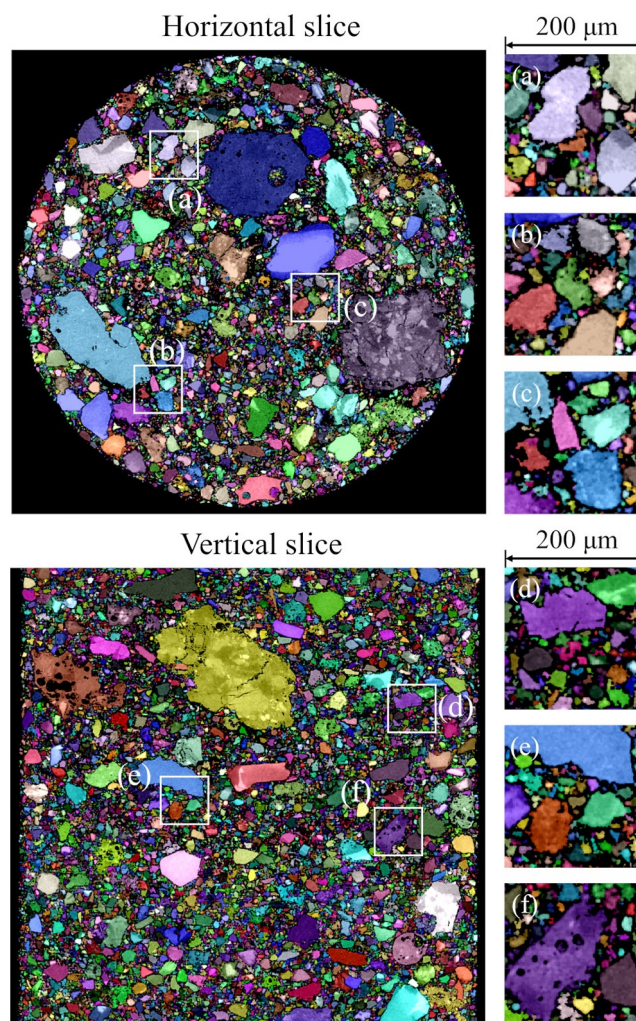


**Figure 5.** Example segmented lunar regolith particles in horizontal and vertical slices of micro-CT scans. Randomly assigned pseudo-color labels of individual lunar regolith particles are superimposed transparently on the grayscale image for illustration of the segmentation results.

micro-CT images. The segmented regions were labeled sequentially, enabling the volume extraction of any arbitrary particle through traversal. A dataset (Wu et al., 2025) was established to store, organize, and manage the data of these particles. This is the first dataset with high-resolution micro-CT images of such a large number of lunar regolith particles. This dataset helps extract grain-scale information of the CE-5 samples and provides a comprehensive understanding of the properties of lunar regolith.

To quantitatively evaluate the accuracy of our segmentation methods, manual inspections were performed on the machine learning-based segmentation results. For example, we found 29 inaccurate segmentations in Figures 5(a–f) from 371 segmented particles mostly on small particles that suffer from the partial volume effect. This shows that the accuracy of our machine-learning-based segmentation is around 92.2%, with almost perfect segmentation performance for large particles.

### 3.2. Particle Size Distribution

Particle size distribution is a fundamental physical property of the lunar regolith that significantly influences its mechanical and thermal behaviors. To obtain the particle size distribution of the CE-5 samples, we calculated the equivalent diameters of all the 710,226 particles segmented from the micro-CT images. The particle size distribution obtained by image segmentation (Figure 6a) revealed that the size of CE-5 lunar regolith particles ranges



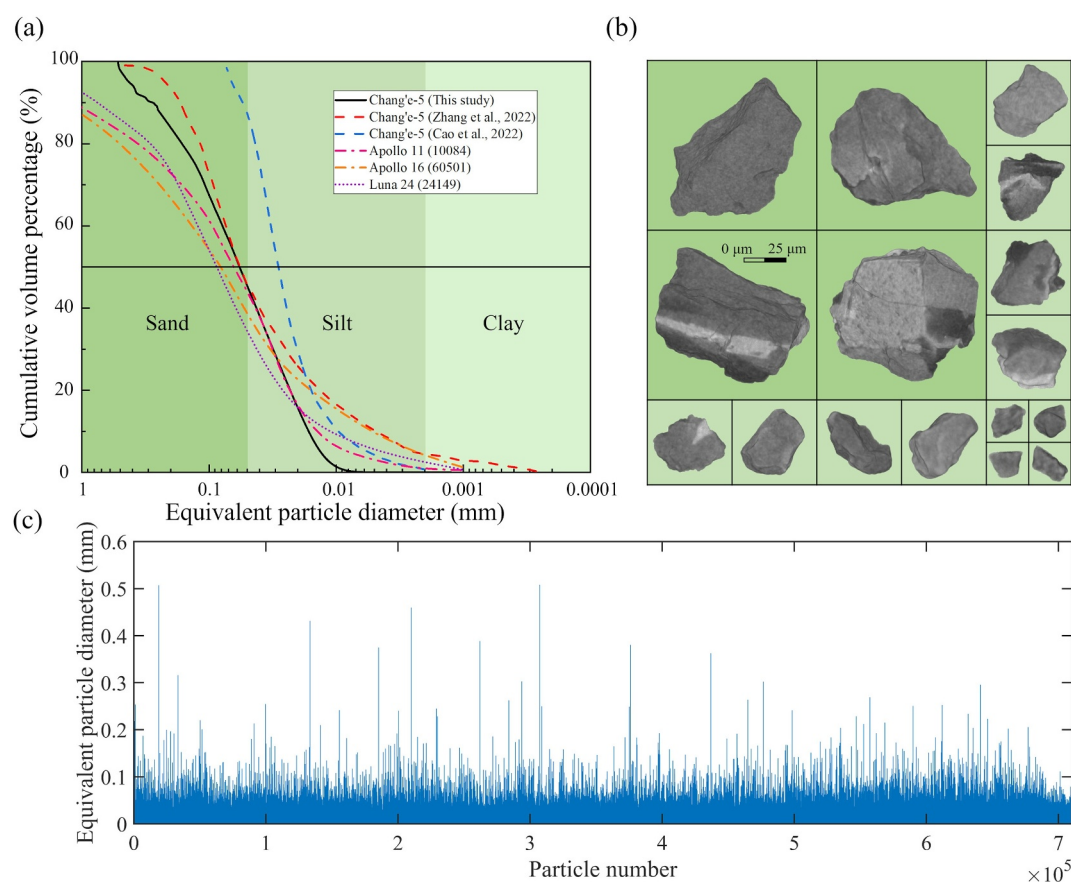


**Figure 6.** Particle size distribution of the CE-5 lunar regolith sample and representative particles with different sizes. (a) Cumulative volume distribution versus equivalent particle diameter of the CE-5 lunar regolith particles determined by our micro-CT imaging technique and other methods (Cao et al., 2022; H. Zhang et al., 2022). The particle size distributions of Apollo 11, Apollo 16 and Luna 24 (Graf, 1993) are also presented for comparison. (b) Examples of segmented volumes of sand- and silt-sized particles. (c) The equivalent particle diameter for all 710,226 particles extracted from micro-CT images.

from fine dust ( $< 5 \mu\text{m}$ ) to large fragments ( $> 100 \mu\text{m}$ ) with a median particle size of  $57.5 \mu\text{m}$  (Figure 6a), which is smaller than Apollo 11 (mature/submature), Apollo 16 (mature), and Luna 24 (immature) samples. Several sand- and silt-sized lunar regolith particles are shown in Figure 6b as examples, further illustrating the dispersed size of lunar regolith particles. In geotechnical terms, the CE-5 lunar regolith sample could be classified as sandy silt or silty sand.

### 3.3. Density Estimation and Mineral Characterization

The correlation between material densities and voxel intensities was established based on the introduced calibration methods, providing the estimated density distribution of the digital volume (Figure 7a). The spatial density distribution could be used to characterize and identify minerals in lunar regolith particles. The lunar soil particles from the CE-5 mission can be broadly categorized into the following types based on the classification criteria of Heiken et al. (1991) and Katagiri et al. (2015): irregular agglutinate particles with internal vesicles, polymineralic particles and monomineralic particles (Figure 7c). For instance, Figure 7b provides a detailed view of a fragmented polymineralic particle with parallel veins showing the presence of four phases with distinct densities. The alternating phases with vein-like patterns can be inferred as pyroxene-ilmenite pairs, which is a typical indicator of shock compression related to an impact event (Tomioka & Fujino, 1997). Based on the estimated density distribution (Figure 7d) and the range of densities of known minerals, these four phases could be identified as ilmenite, pyroxene, plagioclase, and fractures.

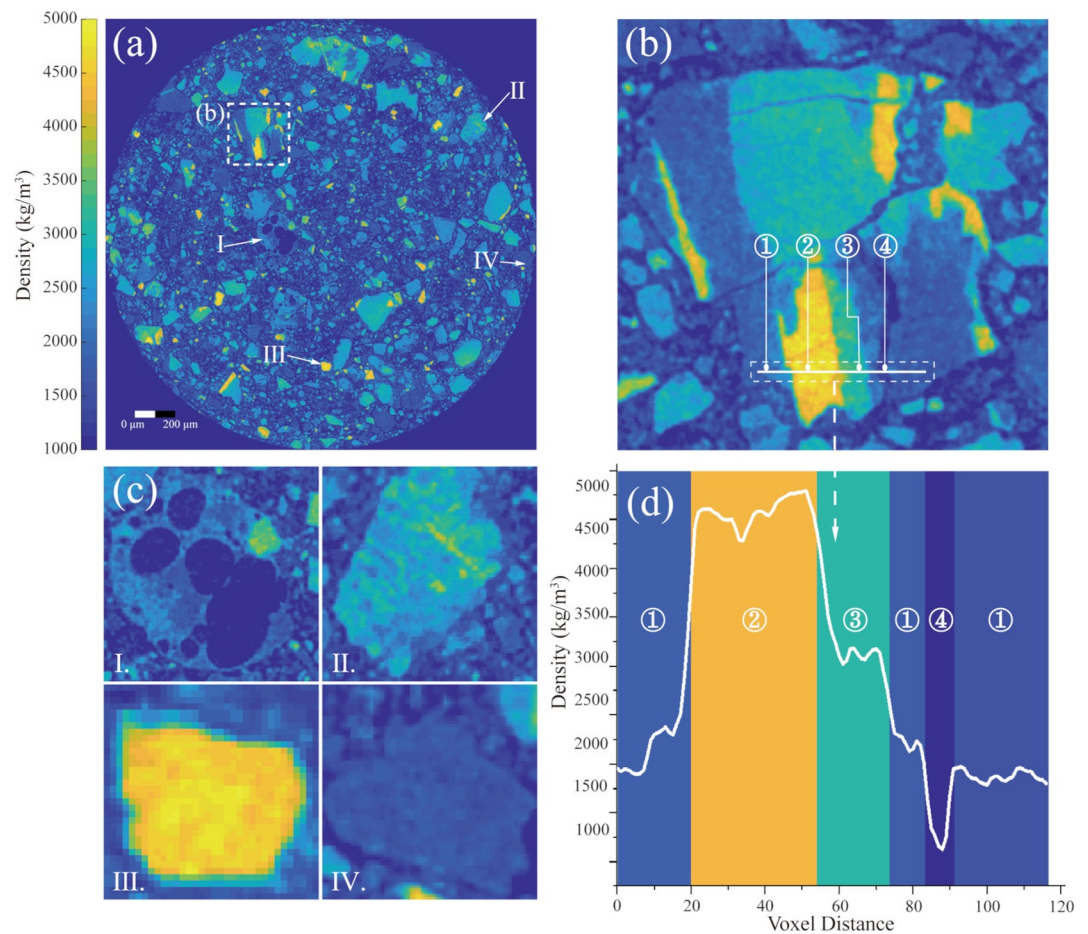


**Figure 7.** Density calibration and phase identification based on micro-CT images. (a) Estimated density distribution in a micro-CT slice. (b) Phase-contrast features zoomed in from (a), where phases 1–4 correspond to plagioclase, ilmenite, pyroxene, and void (fracture), respectively. (c) Representative lunar regolith particles with distinguished types of mineralogical textures including agglutinate (I), polymineralic (II) and monomineralic (III & IV) particles. (d) The profile of estimated density along the white line in panel (b).

The density distribution can also contribute to revealing the 3D microstructural features of lunar regolith particles in the CE-5 sample. By thresholding the estimated density distribution, phase-induced features could be extracted. Figure 8a, Figures 8b and 8c present the 3D structure of a polymineralic particle with an ilmenite vein, a glass particle with several isolated vesicles and a fragmented breccia particle, respectively.

The spatial density distribution derived from micro-CT images enabled the density estimation of individual lunar regolith particles (Figure 9a), allowing for further evaluation of both bulk density ( $1.58 \text{ g/cm}^3$ ) and true density ( $3.17 \text{ g/cm}^3$ ) of the CE-5 sample. It should be noted that bulk density refers to the mass of the lunar regolith per unit volume, including both the particles and the voids, and true density refers to the mass of the lunar regolith per unit volume of the solids alone, excluding both internal pores within the particles and external voids between them. These measurements align with the density values obtained through laboratory measurements (H. Zhang et al., 2022), indicating the accuracy of our methods.

Based on the known types of minerals and the range of mineral densities (Tian et al., 2021), the mineral content (wt.%) of the CE-5 samples can be assessed by thresholding the estimated density distribution (Table 1). It should be noted that some minerals with similar densities were combined as one category. The overall assessment of mineralogy is consistent with previous measurements (Cao et al., 2022; C. Li et al., 2022; Qian et al., 2023; Zhang et al., 2022).

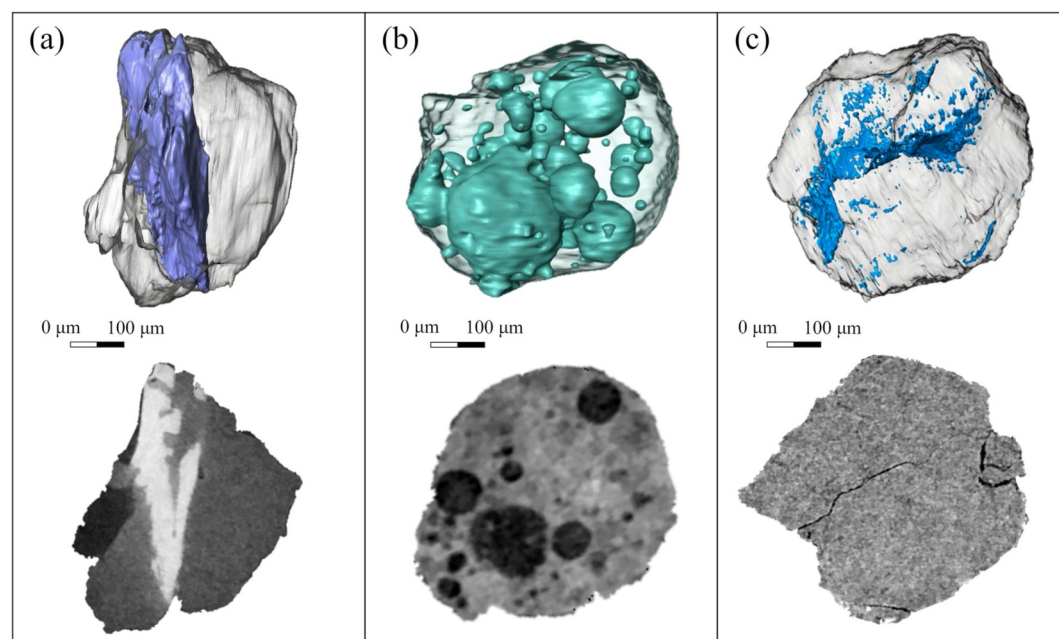


**Figure 8.** 3D structures of three typical lunar regolith particles and representative micro-CT slices. (a) A polyminerallc particle with high-density ilmenite (in purple). (b) A glass particle with isolated vesicles (in green). (c) Breccia particle with fractures (in blue).

### 3.4. Shape Characteristics of Lunar Regolith Particles

To quantify the shape characteristics of lunar regolith particles and minimize errors introduced by voxelization, spherical harmonics and form ratios were computed for 20,396 particles that have volumes larger than 15,000 voxels, which is approximately equivalent to the shortest dimension of 20  $\mu\text{m}$ . The triangular surface meshes of the particles were generated and saved in surface mesh (STL) files. STL files (Figure 10a) using the open-source code iso2mesh (Fang & Boas, 2009).

Spherical harmonic analysis was conducted with a maximum SH degree of 25. It was found that a satisfactory reconstruction could be achieved when the SH degree  $n > 15$  by comparing the reconstructed particle shapes at different SH degrees with the actual particle shape (Figure 10a). The statistical analysis (Figure 10b) reveals a linear correlation between the mean SH descriptors and the SH degree in log-log scales (Figure 10b), demonstrating the self-similarity of multiscale morphological features of lunar regolith particles. Our results indicate

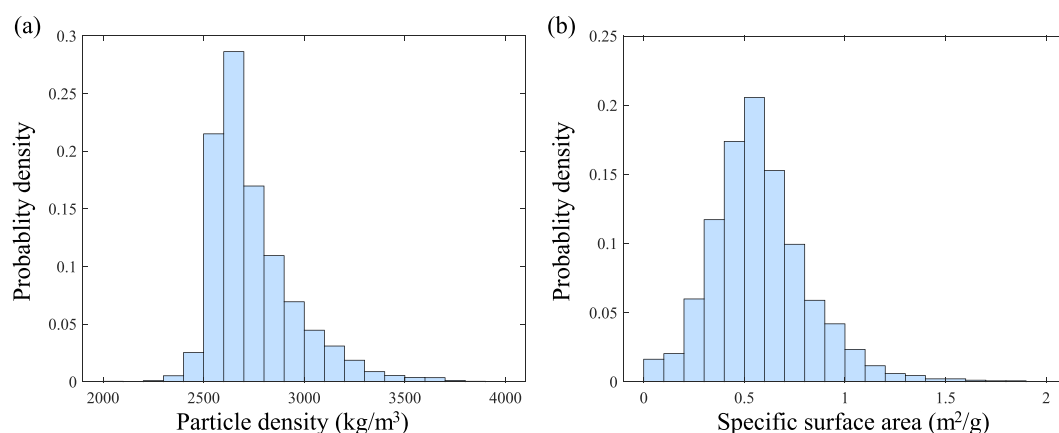


**Figure 9.** Probability density distribution of properties of lunar regolith particles segmented from micro-CT images. (a) Histogram of particle density. (b) Histogram of specific surface area.



**Table 1**

*Mineral Content of CE-5 Lunar Regolith Samples Obtained From Micro-CT Imaging Compared With Previous Laboratory Measurements (Cao et al., 2022; C. Li et al., 2022; Qian et al., 2023; H. Zhang et al., 2022)*

Sources	Methods	Glass/Plagioclase	Pyroxene/Olivine	Ilmenite
C. Li et al. (2022)	XRD	46.7%	47.7%	4.5%
H. Zhang et al. (2022)	XRD	45.9%	48.1%	6.0%
Cao et al. (2022)	Raman	49.7%	42.3%	3.3%
Qian et al. (2023)	Raman	38.9%	55.9%	5.2%
Our study	Micro-CT	45.6%	49.7%	4.7%

that CE-5 particles exhibit the highest SH descriptors among the three types of particles. According to Equation 9, linear fitting was performed for  $\log(D_n)$  versus  $\log(n)$  of three types of particles (Figure 10b). Based on the fitting parameters, the mean fractal dimension  $FD$  of CE-5, HDG and LBS particles were calculated to be 2.32, 2.28, and 2.11, respectively. The reconstruction of the particle surface also allows for the estimation of the specific surface area of each lunar regolith particle (Figure 9b). The mean value of the specific surface area is found to be  $0.59 \text{ m}^2/\text{g}$ , which is close to the previous result ( $0.56 \text{ m}^2/\text{g}$ ) from C. Li et al. (2022).

The form factors of the 20,396 lunar soil particles are shown in Figure 11a. The mean elongation index ( $EI$ ), flatness index ( $FI$ ), and aspect ratio ( $AR$ ) were found to be 0.7322, 0.7786, and 0.5679, respectively. Size dependency was observed by calculating the moving average of  $AR$  as a function of the intermediate particle length ( $I$ ), which serves as a representative measure of particle size. The  $AR$  initially increases and reaches a peak at approximately  $40 \text{ }\mu\text{m}$ , after which it declines with observable fluctuations around the mean value (Figure 11b). Considering that the form factor is size-dependent, the CE-5 samples were divided into four particle size groups for the comparison with Luna and Apollo samples (Tsuchiyama et al., 2022). The mean form factors are shown as Zingg diagrams (Figure 12), where  $EI$  is plotted against  $FI$ . Our results demonstrate that data points of CE-5 are further left and lower in the diagram compared to other samples regardless of particle size, indicating a smaller aspect ratio and a less spherical shape.

#### 4. Discussion

In this study, we quantitatively evaluated several critical physical properties of CE-5 lunar regolith samples using micro-CT imaging. Our results generally agree with previous studies with slight differences possibly due to differences among different batches of samples and varying measurement methods. The blue and red dashed curves in Figure 6a represent the measurements of Cao et al. (2022) using Raman particle analysis and H. Zhang et al. (2022) using laser diffraction, respectively. The obtained median particle size in our study is  $57.5 \text{ }\mu\text{m}$ , close to  $55.24 \text{ }\mu\text{m}$  from H. Zhang et al. (2022) and larger than  $28.4 \text{ }\mu\text{m}$  from Cao et al. (2022). We also found that particles smaller than  $10 \text{ }\mu\text{m}$  accounted for only 1.4% of the total volume in our segmentation. However, H. Zhang et al. (2022) and Cao et al. (2022) reported volume fractions of approximately 17.0% and 10.8% for particles under  $10 \text{ }\mu\text{m}$ , respectively. This is attributed to the limited spatial resolution of micro-CT images, which poses challenges in accurately identifying very fine particles. The median particle size would be  $73.6 \text{ }\mu\text{m}$  for H. Zhang et al. (2022) and  $30.7 \text{ }\mu\text{m}$  for Cao et al. (2022) with a cutoff particle size of  $10 \text{ }\mu\text{m}$ .

The obtained median particle size of the CE-5 samples is smaller than that of the Apollo 11, Apollo 16 and Luna 24 samples (Carrier III, 1973; Duke et al., 1970; Graf, 1993; Hapke, 1968). The particle size distribution is widely used to quantify the maturity of lunar regolith samples. Generally, a smaller median particle size is associated with a higher degree of maturity (Y. Chen et al., 2023; C. Li et al., 2022; H. Zhang et al., 2021). However, the immature lunar soil samples from the Luna 24 mission exhibit a larger median grain size compared to the mature samples from Apollo 11 and Apollo 16. This counterexample indicates that median grain size alone is insufficient to determine the maturity of lunar regolith samples. The particle size of lunar regolith might not be monotonically correlated with maturity as the space weathering effect on the particle size was controlled by the competing effects of micrometeorite comminution and agglutination (McKay et al., 1974). Moreover, the particle size of lunar regolith is significantly determined by the intrinsic crystal size of the protolith, which is influenced by the cooling

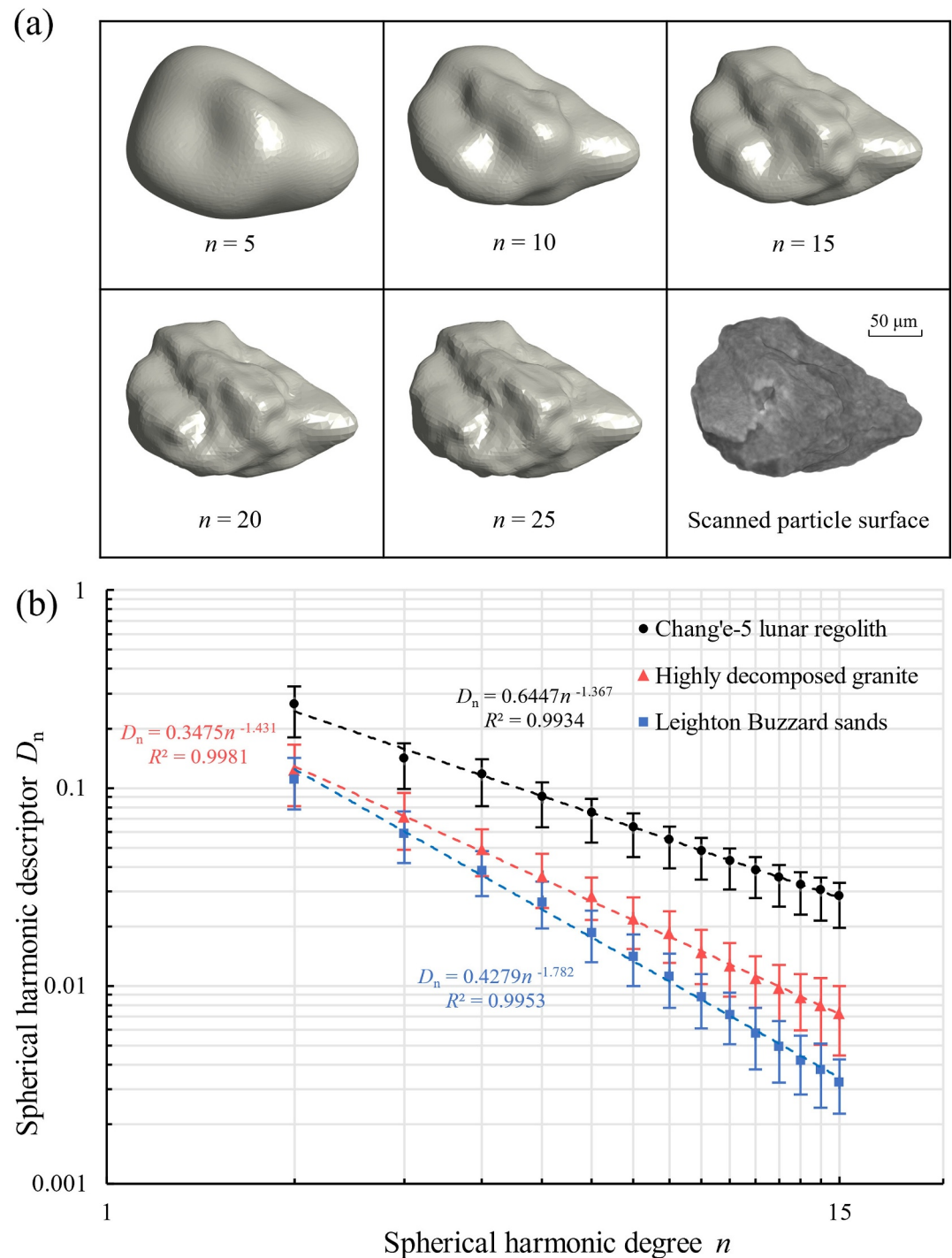


**Figure 10.** Spherical harmonic (SH) analysis of CE-5 lunar regolith particles. (a) Comparison between scanned particle surface and reconstructed particle surface with different degrees of spherical harmonics ( $n$  from 5 to 25). (b) SH descriptors as a function of the SH degree  $n$  for CE-5 lunar regolith particles and two types of terrestrial soils. Data of Leighton Buzzard sand (LBS) and highly decomposed granite (HDG) are from Wei, Wang, Nie, and Zhou (2018), Wei, Wang, and Zhao (2018).

rate and the chemical composition of the magma (Head & Wilson, 2020; Qian et al., 2024). He et al. (2022) suggested that CE-5 basalts may experience rapid cooling after eruption, which may explain the relatively small particle size of CE-5 samples.

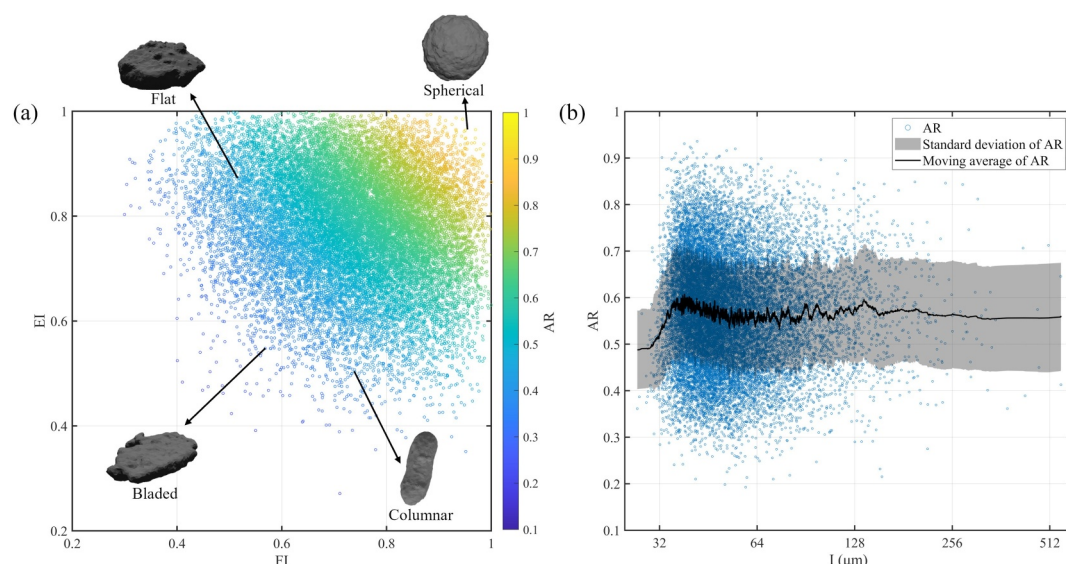


**Figure 11.** Form factors distributions of CE-5 lunar regolith particles. (a) Zingg diagrams of CE-5 lunar regolith particles displaying distributions of  $EI$ ,  $FI$ , and aspect ratios ( $AR$ ). (b) The relationship between  $AR$  and the intermediate length ( $I$ ) reveals size dependency of particle shape. The moving average of  $AR$  is plotted with shaded error bars indicating the standard deviation.

The assessment of mineral content in our study is consistent with previous research using X-ray diffraction (XRD) (C. Li et al., 2022; H. Zhang et al., 2022), which is a mature technique for identifying crystalline phases and quantifying their abundance. However, XRD relies on the identification of each phase, which may not always be trivial. For example, XRD is unsuitable for amorphous materials (e.g., glass) and trace amount phases (<0.1%–1.0%) may be undetected (McCusker et al., 1999). In addition, quantitative analysis of mineral content is inferred from XRD patterns instead of direct measurement. Our study relies on the 3D volumetric representation of the particles and the correlation between density and the level of X-ray attenuation in materials. This provides a non-destructive and direct measurement approach to evaluate the mineral content of lunar regolith samples with digital images. Although minerals of similar densities (i.e., glass/plagioclase and pyroxene/olivine) can hardly be distinguished, and the accurate mineral composition (e.g., EnFsWo in pyroxene) cannot be assessed by micro-CT images, the combined proportions of glass/plagioclase and pyroxene/olivine as well as the proportion of ilmenite still provide valuable verification for measurements from other techniques. In addition, the spatial relations between different minerals and their morphological characteristics may also aid in identifying mineral phases.

Visualization and characterization of specific particles in the CE-5 samples could provide us with a massive amount of information about the geologic history of the sampling sites. Based on micro-CT images of CE-5 samples, we identified agglutinate particles, polymineralic particles and monomineralic particles, which were classified by Heiken et al. (1991) and Katagiri et al. (2015). This finding demonstrates that the CE-5 sample exhibits considerable similarity to other lunar regolith samples in terms of mineralogical textures. Q.-L. Li et al. (2021) and Qian et al. (2024) proposed that the agglutinate abundance (~16.6%) in CE-5 soil is lower than that observed in all Apollo mature soils (>30%), which may indicate the immaturity based on the established correlation between agglutinate abundance and soil maturity.

The observed high-intensity phases (Figure 8a) confirmed the existence of mineral composition with high-density metal elements such as Fe and Ti. The vesicles in the glass particle (Figure 8b) may have been formed when dissolved gases bubble out of the magma as it decompresses during its approach to the surface and lava solidifies before the gases can escape (Blatt et al., 2006; W. Yang et al., 2022; Y. Yang et al., 2022). This glass particle may also imply past high-temperature events such as meteorite impacts, which can generate similar features by rapidly melting the surrounding material and trapping gases in the process. The fragmentation of lunar regolith particles (Figure 8c) could be induced by several stress-related processes in many ways, including temperature change, application and release of overburden pressure, shearing forces, crystal growth, water pressure, or tension (Steiglitz, 1988).



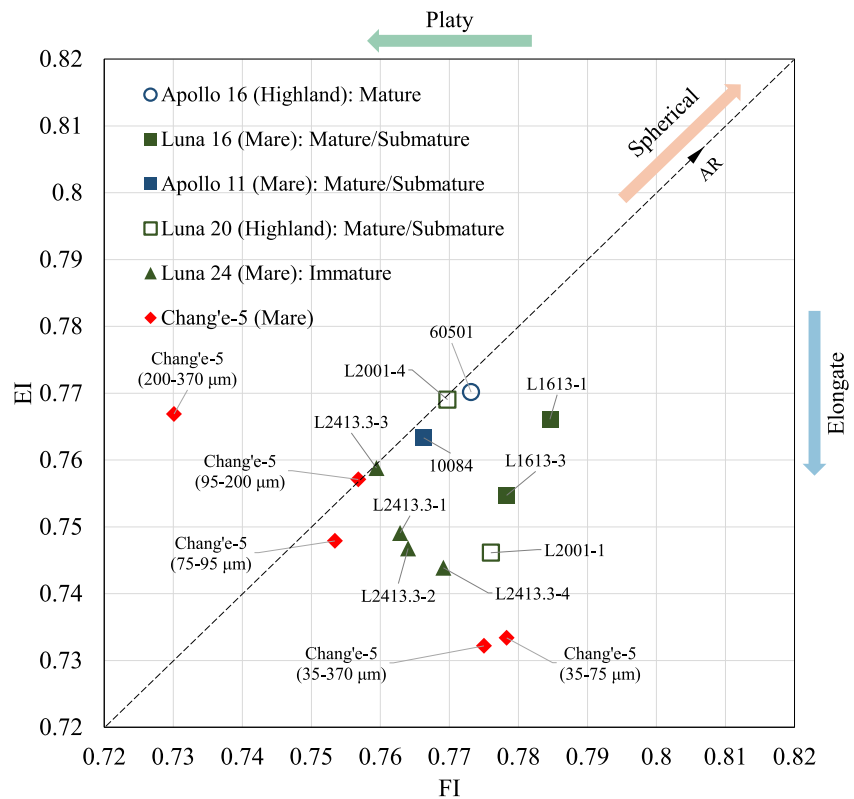


**Figure 12.** Zingg diagrams showing the mean form factors of CE-5 lunar regolith particles and comparisons with samples from Luna and Apollo missions (detailed sample information in Table S2 in Supporting Information S1).

In order to compare the shape characteristics of lunar regolith particles and terrestrial geomaterials, the spherical harmonics data of Leighton Buzzard sand (LBS) and highly decomposed granite (HDG) sourced from Wei, Wang, Nie, and Zhou (2018), Wei, Wang, and Zhao (2018) are also included in Figure 10b. The LBS have rounded and smooth particle surfaces because of geological transportation processes, while the HDG are typically angular and rough and have numerous surface asperities. Our results suggest that lunar regolith particles exhibit the largest SH descriptors  $D_n$  among the three types of geomaterials, while HDG displays larger SH descriptors than LBS. This result indicates that lunar regolith particles exhibit more complex morphological features with more angular shapes, sharper edges and finer textures compared with LBS and HDG (Figure 10b). The SH descriptors  $D_n$  shift from capturing the overall shape to detailing surface roughness as the SH degree  $n$  increases. The fractal dimension  $FD$  which is calculated from the slope of  $\log(D_n)$  versus  $\log(n)$  describes the complexity and self-similarity of particle shapes. A low  $FD$  indicates that the particle shape is relatively smooth and less textured. It also suggests a low self-similarity, which means the particle surface does not have the same level of fine structural details or variations seen in particles with higher fractal dimensions. The particle shape of sandy soils and sedimentary deposits on Earth is primarily influenced by several geomorphological processes that involve various physical, chemical, and biological mechanisms over an extended period of time (Crook, 1968; Hiebert & Bennett, 1992). For instance, LBS is classified as a transported soil that mainly experiences geological transportation processes with dissolution or chemical alteration, resulting in rounded and smooth particle surfaces. This leads to the lowest  $FD$  among the three types of particles. In contrast, the shape of HDG particles is controlled by the initial fragmentation and erosion of granite rocks over an extended period as typical residual soils, which remain sub-angular to angular and slightly rough Wei, Wang, Nie, & Zhou, 2018, Wei, Wang, & Zhao, 2018. Thus, HDG has a larger  $FD$  compared to LBS. However, the space weathering on the Moon is distinct from the weathering on the Earth. Dissolution or chemical alteration of mineral composition is absent on the Moon surface. Additionally, there are no biological processes contributing to weathering on the Moon due to the absence of life. Instead, the evolution of the lunar regolith is primarily affected by micrometeorite impacts, constant radiation of cosmic rays, and extreme temperature variation over billions of years of geological time

(Anand et al., 2004; Colwell et al., 2007). Constant radiation of the solar wind and cosmic rays shape (Lacznia et al., 2021; Thompson et al., 2016) the particle morphology in nano-scale. Thus, the surface morphology of lunar regolith at the resolution of micro-CT imaging is dominant by micrometeorite impacts, which lead to fracturing, fragmentation, melting and vapourization (Gu et al., 2022; M. Zhang et al., 2023) and also cause mechanical abrasion (Tsuchiyama et al., 2022). Most CE-5 particles possess angular and rough shapes after a long period of space weathering as shown in Figure 5, which is evident by a higher *FD* compared to those of HDG and LBS.

Form factors could describe the overall shape of lunar regolith particles and is regarded as another potential indicator of maturity. Michikami et al. (2018) demonstrated that fresh basalt fragments produced by hypervelocity impact experiments have a lower mean aspect ratio compared to lunar regolith particles. Our results revealed that the CE-5 particles exhibit a lower mean aspect ratio compared to other lunar samples, with a tendency toward less spherical shapes, indicating similar immaturity to Luna 24 samples (Figure 12). The morphological evolution of lunar regolith particles is controlled by the competing effects of impact fragmentation and mechanical abrasion during long-term space weathering. Fragmentation of regolith particles occurs under intense dynamic loading (Huang et al., 2016, 2018) induced by a large meteorite striking the lunar surface with a high velocity, generating strong shock waves that cause particle crushing of lunar regolith near the impact site. In contrast, abrasion occurs under dynamic loading conditions with relatively low energy (Xiao et al., 2019), such as those produced by smaller meteorites with slower impact velocities or shock waves that have propagated from a distant impact site. In these scenarios, the shock waves are insufficient to cause substantial fragmentation but adequate to induce frictional sliding between particles, leading to the wearing and smoothing of the particle surface. Thus, the relatively low *AR* of CE-5 particles may not necessarily suggest that they are immature, as they might experience a significant number of high-intensity impact events, which would also lead to a lower *AR*. More accurate constraints on the impact-induced morphological modification of irregularly shaped particles require future investigations.

The particle shape characteristics of the lunar regolith have multiple influences on its overall behavior. Granular assemblies composed of particles with smaller aspect ratios are likely to exhibit stronger fabric anisotropy, which plays a crucial role in the mechanical and thermal behavior of lunar regolith (J. Chen et al., 2024). Irregularly shaped particles with rough surfaces can interlock more effectively allowing for higher interparticle friction than weathered terrestrial particles. This is closely related to the compressibility of the particles, which affects the thermal conductivity and wave velocity (Lee et al., 2017). The lunar regolith layer may have lower shear wave velocity than weathered terrestrial soils of similar composition. This is due to the Moon's gravity being only 1/6 of Earth's gravity, and the irregular shapes of lunar particles lead to larger void spaces and fewer particle contacts. Considering the influence of particle shape on the propagation of seismic waves could enhance our understanding of lunar seismic activities and the resultant ground motion (Amrouche et al., 2022; Watters et al., 2019). The morphology of particles plays a significant role in the frictional behavior of granular assemblies especially under low-stress conditions (Cavarretta et al., 2010; Cho et al., 2006; Katagiri et al., 2015; Rousé et al., 2008). This may also be important for the understanding of coseismic landslides on the Moon (Schmitt et al., 2017). Katagiri et al. (2015) proposed that an increased content of agglutinate enhances the shear strength of lunar regolith. Qian et al. (2024) demonstrated a correlation between agglutinate content and regolith maturity. These observations may suggest that different regolith maturities may be associated with varying shear strengths, potentially due to the differing levels of agglutinate present. The shape of the particles may also contribute to the lower thermal conductivity of the lunar regolith, which in turn affects the Moon's subsurface temperature (Woods-Robinson et al., 2019). Moreover, thermal conductivity is a crucial factor for future in situ resource utilization strategies, such as the sintering of lunar regolith (Han et al., 2022).

The number of samples examined has a significant impact on revealing statistical patterns of the lunar regolith particles. Taking the flatness index (*FI*) as an example, our analysis reveals that with the increase in particle number, the mean *FI* exhibits significant fluctuations (Figure 13). This variability can be attributed to the insufficient particle number, where the presence of outliers or unique particles exerts a disproportionate effect on the calculated mean values. These fluctuations diminish as the particle number increases to more than 1,000, where the mean value of *FI* gradually stabilizes within a 5% standard deviation. This trend reflects the sensitivity of shape parameters to sample size, emphasizing the need for a sufficiently large number of particles to achieve reliable and consistent statistical measures. Therefore, it is essential to determine the optimal particle number that balances the need for statistical reliability and the practical constraints of sample collection and analysis. Our findings underscore the importance of considering the number of particles in studies of lunar regolith

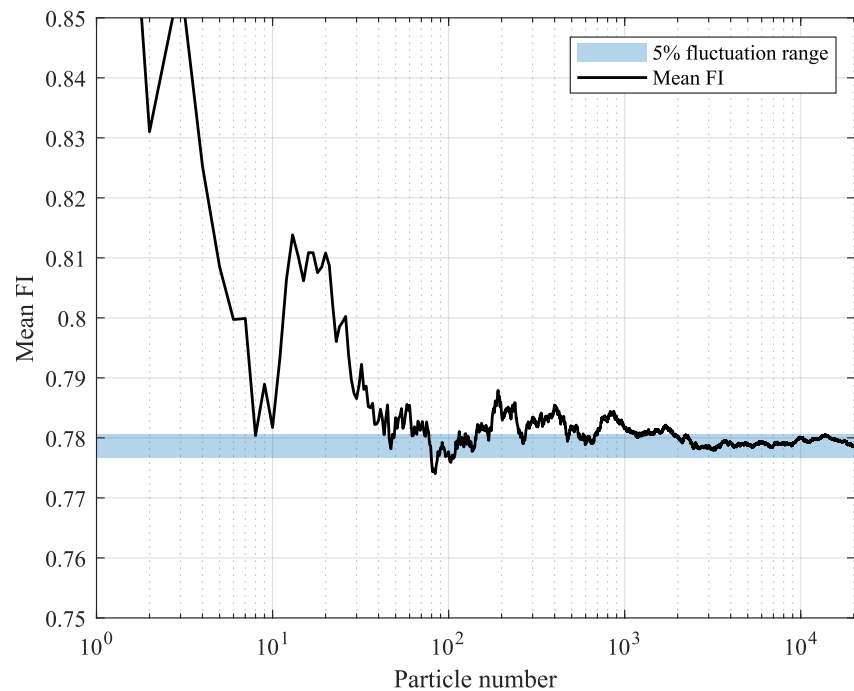


**Figure 13.** Influence of the total particle number on the measurement of mean flatness index (*FI*). The error bar represents the range within which the mean *FI* fluctuates by up to 5%.

characteristics. In this study, we use a micro-CT image segmentation method, which allows us to obtain information on a vast number of particles, ensuring that conclusions drawn about the CE-5 lunar regolith samples are based on robust and representative data.

Lastly, our segmentation methods demonstrate a significant improvement over traditional segmentation methods, particularly in terms of handling complex features and high noise level images. Future work could focus on refining the segmentation to further reduce over-segmentation and under-segmentation, potentially through the incorporation of advanced techniques such as deep learning and post-processing steps. Since various image segmentation methods are currently available and future advancements are anticipated, the micro-CT data provided in our study offer a chance for future comparison and further iterations.

## 5. Conclusions

This study introduces a non-destructive method for characterizing the lunar regolith sample returned by the CE-5 mission using micro-CT imaging and machine learning-based segmentation. We generated and analyzed a comprehensive data set of over 700,000 CE-5 lunar regolith particles, several orders of magnitude larger than previous studies, which significantly enhanced our ability to observe and characterize CE-5 lunar regolith particles. Our study indicates that the CE-5 samples have a median particle size of 57.5  $\mu\text{m}$ , smaller than Apollo 11, Apollo 16, and Luna 24 samples. By comparing CE-5 lunar regolith particles with both terrestrial soils and other lunar samples, we revealed their less spherical shape with more complex morphological features.

Several pieces of evidence point to contradicting levels of maturity of the CE-5 lunar regolith. Compared to the previous lunar regolith sample, the smaller median particle size indicates higher maturity; however, the less spherical shape and the observed low agglutinate abundance suggest a relatively immature regolith. We recommend that due to the variability of the intrinsic crystal size of the protolith and the complexity of processes involved in space weathering, the relationship between lunar regolith particle size and morphology and maturity should be evaluated with caution, appealing further constraints to accurately assess the maturity of lunar regolith. In addition, we found that the number of examined particles should be sufficiently large ( $>1,000$ ) to obtain reliable shape and size characteristics. This study validates the feasibility and effectiveness of our proposed



micro-CT imaging-based method for the examination of million-scale extraterrestrial soil particles, which provides a non-destructive approach for assessing mineral components of precious extraterrestrial samples in future deep space explorations.

## Data Availability Statement

Raw and segmented image data as well as particle morphology data are available in the Figshare repository located at Wu et al. (2025).

## Acknowledgments

We appreciate the constructive suggestions and comments from the editor, Dr. Takashi Matsushima and anonymous reviewers. Q. Zhao, H. Wu, and Y. Zou are supported by projects of the PolyU Research Centre for Deep Space Explorations (P0049221 and P0041304). B. Wu is supported by the Research Grants Council of Hong Kong (RIF Project No: R5043-19W). W. Yang would like to thank the support from the National Natural Science Foundation of China (42241103) and the Key Research Program of Institute of Geology and Geophysics, Chinese Academy of Sciences (IGGCAS-202101).

## References

- Amrouche, M., Weber, R. C., Schmerr, N., & Iqbal, W. (2022). Effects of lunar near-surface geology on moonquakes ground motion amplification. *Journal of Geophysical Research: Planets*, 127(9), e2022JE007396. <https://doi.org/10.1029/2022JE007396>
- Anand, M., Taylor, L. A., Nazarov, M. A., Shu, J., Mao, H.-K., & Hemley, R. J. (2004). Space weathering on airless planetary bodies: Clues from the lunar mineral hapkeite. *Proceedings of the National Academy of Sciences*, 101(18), 6847–6851. <https://doi.org/10.1073/pnas.0401565101>
- Andres, B., Kappes, J. H., Beier, T., Köthe, U., & Hamprecht, F. A. (2011). Probabilistic image segmentation with closedness constraints. *2011 International Conference on Computer Vision*, 2611–2618. <https://doi.org/10.1109/ICCV.2011.6126550>
- Blatt, H., Tracy, R., & Owens, B. (2006). *Petrology: Igneous, sedimentary, and metamorphic*. Macmillan.
- Borg, L. E., Connelly, J. N., Boyet, M., & Carlson, R. W. (2011). Chronological evidence that the Moon is either young or did not have a global magma ocean. *Nature*, 477(7362), 70–72. <https://doi.org/10.1038/nature10328>
- Breiman, L. (2001). Random forests. *Machine Learning*, 45(1), 5–32. <https://doi.org/10.1023/A:1010933404324>
- Cao, K., Dong, M., She, Z., Xiao, Q., Wang, X., Qian, Y., et al. (2022). A novel method for simultaneous analysis of particle size and mineralogy for Chang'e-5 lunar soil with minimum sample consumption. *Science China Earth Sciences*, 65(9), 1704–1714. <https://doi.org/10.1007/s11430-022-9966-5>
- Carrier, W. D. III. (1973). Lunar soil grain size distribution. *The Moon*, 6(3–4), 250–263. <https://doi.org/10.1007/BF00562206>
- Carrier, W. D. III, Bromwell, L. G., & Torrence Martin, R. (1972). Strength and compressibility of returned lunar soil. *Lunar and Planetary Science Conference Proceedings*, 3, 3223.
- Cavarretta, I., Coop, M., & O'Sullivan, C. (2010). The influence of particle characteristics on the behaviour of coarse grained soils. *Géotechnique*, 60(6), 413–423. <https://doi.org/10.1680/geot.2010.60.6.413>
- Chang, R., Lin, H., Yang, W., Ruan, R., Liu, X., Tian, H.-C., & Xu, J. (2023). Comparison of laboratory and in situ reflectance spectra of Chang'e-5 lunar soil. *Astronomy & Astrophysics*, 674, A68. <https://doi.org/10.1051/0004-6361/202245751>
- Chen, J., Zhao, C., Chen, Y., & Yang, Z. (2024). Effects of particle overall regularity and surface roughness on fabric evolution of granular materials: DEM simulations. *International Journal for Numerical and Analytical Methods in Geomechanics*, 48(13), 3284–3307. <https://doi.org/10.1002/nag.3792>
- Chen, Y., Hu, S., Li, J.-H., Li, Q.-L., Li, X., Li, Y., et al. (2023). Chang'e-5 lunar samples shed new light on the Moon. *The Innovation Geoscience*, 1(1), 100014. <https://doi.org/10.59717/j.xinn-geo.2023.100014>
- Chen, Y., Ma, G., Zhou, W., Wei, D., Zhao, Q., Zou, Y., & Grasselli, G. (2021). An enhanced tool for probing the microscopic behavior of granular materials based on X-ray micro-CT and FDEM. *Computers and Geotechnics*, 132, 103974. <https://doi.org/10.1016/j.compgeo.2020.103974>
- Chiaromonti, A. N., Goguen, J. D., & Garboczi, E. J. (2017). Quantifying the 3-dimensional shape of lunar regolith particles using X-ray computed tomography and scanning electron microscopy at sub- $\gamma$  resolution. *Microscopy and Microanalysis*, 23(S1), 2194–2195. <https://doi.org/10.1017/S1431927617011631>
- Cho, G.-C., Dodds, J., & Santamarina, J. C. (2006). Particle shape effects on packing density, stiffness, and strength: Natural and crushed sands. *Journal of Geotechnical and Geoenvironmental Engineering*, 132(5), 591–602. [https://doi.org/10.1061/\(ASCE\)1090-0241\(2006\)132:5\(591\)](https://doi.org/10.1061/(ASCE)1090-0241(2006)132:5(591))
- Colwell, J. E., Batiste, S., Horányi, M., Robertson, S., & Sture, S. (2007). Lunar surface: Dust dynamics and regolith mechanics. *Reviews of Geophysics*, 45(2), 2005RG000184. <https://doi.org/10.1029/2005RG000184>
- Costes, N. C., Cohron, G. T., & Moss, D. C. (1971). Cone penetration resistance test—an approach to evaluating in-place strength and packing characteristics of lunar soils. *Proceedings of the Lunar Science Conference*, 2, 1973.
- Crook, K. A. W. (1968). Weathering and roundness of quartz sand grains. *Sedimentology*, 11(3–4), 171–182. <https://doi.org/10.1111/j.1365-3091.1968.tb00851.x>
- Deitrick, S. R., & Cannon, K. M. (2022). Characterizing detailed grain shape and size distribution properties of lunar regolith. *53rd Lunar and Planetary Science Conference*. <https://ntrs.nasa.gov/citations/20210026714>
- Duke, M. B., Woo, C. C., Bird, M. L., Sellers, G. A., & Finkelman, R. B. (1970). Lunar soil: Size distribution and mineralogical constituents. *Science*, 167(3918), 648–650. <https://doi.org/10.1126/science.167.3918.648>
- Ellery, A. (2022). Leveraging in situ resources for lunar base construction. *Canadian Journal of Civil Engineering*, 49(5), 657–674. <https://doi.org/10.1139/cjce-2021-0098>
- Fang, Q., & Boas, D. A. (2009). Tetrahedral mesh generation from volumetric binary and grayscale images. *2009 IEEE International Symposium on Biomedical Imaging: From Nano to Macro*, 1142–1145. <https://doi.org/10.1109/ISBI.2009.5193259>
- Fujiwara, A., Kamimoto, G., & Tsukamoto, A. (1978). Expected shape distribution of asteroids obtained from laboratory impact experiments. *Nature*, 272(5654), 602–603. <https://doi.org/10.1038/272602a0>
- Garboczi, E. J. (2002). Three-dimensional mathematical analysis of particle shape using X-ray tomography and spherical harmonics: Application to aggregates used in concrete. *Cement and Concrete Research*, 32(10), 1621–1638. [https://doi.org/10.1016/S0008-8846\(02\)00836-0](https://doi.org/10.1016/S0008-8846(02)00836-0)
- Graf, J. C. (1993). Lunar soils grain size catalog. <https://ntrs.nasa.gov/citations/19930012474>
- Gu, L., Chen, Y., Xu, Y., Tang, X., Lin, Y., Noguchi, T., & Li, J. (2022). Space weathering of the Chang'e-5 lunar sample from a mid-high latitude region on the Moon. *Geophysical Research Letters*, 49(7), e2022GL097875. <https://doi.org/10.1029/2022GL097875>
- Han, W., Ding, L., Cai, L., Zhu, J., Luo, H., & Tang, T. (2022). Sintering of HUST-1 lunar regolith simulant. *Construction and Building Materials*, 324, 126655. <https://doi.org/10.1016/j.conbuildmat.2022.126655>
- Hapke, B. W. (1968). On the particle size distribution of lunar soil. *Planetary and Space Science*, 16(1), 101–110. [https://doi.org/10.1016/0032-0633\(68\)90047-0](https://doi.org/10.1016/0032-0633(68)90047-0)

- He, Q., Li, Y., Baziotis, I., Qian, Y., Xiao, L., Wang, Z., et al. (2022). Detailed petrogenesis of the unsampled Oceanus Procellarum: The case of the Chang'e-5 mare basalts. *Icarus*, 383, 115082. <https://doi.org/10.1016/j.icarus.2022.115082>
- Head, J. W., & Wilson, L. (2020). Rethinking lunar mare basalt regolith formation: New concepts of lava flow protolith and evolution of regolith thickness and internal structure. *Geophysical Research Letters*, 47(20), e2020GL088334. <https://doi.org/10.1029/2020GL088334>
- Heiken, G., Vaniman, D., & French, B. M. (1991). *Lunar sourcebook: A user's guide to the Moon*. CUP Archive.
- Hiebert, F. K., & Bennett, P. C. (1992). Microbial control of silicate weathering in organic-rich ground water. *Science*, 258(5080), 278–281. <https://doi.org/10.1126/science.258.5080.278>
- Huang, X., Qi, S., Xia, K., & Shi, X. (2018). Particle crushing of a filled fracture during compression and its effect on stress wave propagation. *Journal of Geophysical Research: Solid Earth*, 123(7), 5559–5587. <https://doi.org/10.1029/2018JB016001>
- Huang, X., Zhao, Q., Qi, S., Xia, K., Grasselli, G., & Chen, X. (2016). Numerical simulation on seismic response of the filled joint under high amplitude stress waves using finite-discrete element method (FDEM). *Materials*, 10(1), 13. <https://doi.org/10.3390/ma10010013>
- Humbert, L., Hazratí Marangalou, J., del Río Barquero, L. M., van Lenthe, G. H., & van Rietbergen, B. (2016). Technical note: Cortical thickness and density estimation from clinical CT using a prior thickness-density relationship. *Medical Physics*, 43(4), 1945–1954. <https://doi.org/10.1118/1.4944501>
- Katagiri, J., Matsushima, T., Yamada, Y., Tsuchiyama, A., Nakano, T., Uesugi, K., et al. (2015). Investigation of 3D grain shape characteristics of lunar soil retrieved in Apollo 16 using image-based discrete-element modeling. *Journal of Aerospace Engineering*, 28(4), 04014092. [https://doi.org/10.1061/\(ASCE\)AS.1943-5525.0000421](https://doi.org/10.1061/(ASCE)AS.1943-5525.0000421)
- Laczniak, D. L., Thompson, M. S., Christoffersen, R., Dukes, C. A., Clemett, S. J., Morris, R. V., & Keller, L. P. (2021). Characterizing the spectral, microstructural, and chemical effects of solar wind irradiation on the Murchison carbonaceous chondrite through coordinated analyses. *Icarus*, 364, 114479. <https://doi.org/10.1016/j.icarus.2021.114479>
- La Spina, A., & Paolicchi, P. (1996). Catastrophic fragmentation as a stochastic process: Sizes and shapes of fragments. *Planetary and Space Science*, 44(12), 1563–1578. [https://doi.org/10.1016/S0032-0633\(96\)00064-5](https://doi.org/10.1016/S0032-0633(96)00064-5)
- Lee, C., Suh, H. S., Yoon, B., & Yun, T. S. (2017). Particle shape effect on thermal conductivity and shear wave velocity in sands. *Acta Geotechnica*, 12(3), 615–625. <https://doi.org/10.1007/s11440-017-0524-6>
- Lei, L., Seol, Y., & Jarvis, K. (2018). Pore-scale visualization of methane hydrate-bearing sediments with micro-CT. *Geophysical Research Letters*, 45(11), 5417–5426. <https://doi.org/10.1029/2018GL078507>
- Li, C., Hu, H., Yang, M.-F., Pei, Z.-Y., Zhou, Q., Ren, X., et al. (2022). Characteristics of the lunar samples returned by the Chang'E-5 mission. *National Science Review*, 9(2), nwab188. <https://doi.org/10.1093/nsr/nwab188>
- Li, C., Wang, C., Wei, Y., & Lin, Y. (2019). China's present and future lunar exploration program. *Science*, 365(6450), 238–239. <https://doi.org/10.1126/science.aax9908>
- Li, Q.-L., Zhou, Q., Liu, Y., Xiao, Z., Lin, Y., Li, J.-H., et al. (2021). Two-billion-year-old volcanism on the Moon from Chang'e-5 basalts. *Nature*, 600(7887), 54–58. <https://doi.org/10.1038/s41586-021-04100-2>
- Longhi, J. (1992). Experimental petrology and petrogenesis of mare volcanics. *Geochimica et Cosmochimica Acta*, 56(6), 2235–2251. [https://doi.org/10.1016/0016-7037\(92\)90186-M](https://doi.org/10.1016/0016-7037(92)90186-M)
- Lu, X., Chen, J., Ling, Z., Liu, C., Fu, X., Qiao, L., et al. (2023). Mature lunar soils from Fe-rich and young mare basalts in the Chang'e-5 regolith samples. *Nature Astronomy*, 7(2), 142–151. <https://doi.org/10.1038/s41550-022-01838-1>
- Matsushima, T., Katagiri, J., Saiki, K., Tsuchiyama, A., Ohtake, M., Nakano, T., & Uesugi, K. (2008). 3D particle characteristics of highland lunar soil (No. 60501) obtained by micro X-ray CT. In *Earth & space 2008: Engineering, science, construction, and operations in challenging environments* (pp. 1–8).
- McCusker, L. B., Von Dreele, R. B., Cox, D. E., Louër, D., & Scardi, P. (1999). Rietveld refinement guidelines. *Journal of Applied Crystallography*, 32(1), 36–50. <https://doi.org/10.1107/S0021889898009856>
- McKay, D. S., Fruland, R. M., & Heiken, G. H. (1974). Grain size and the evolution of lunar soils. In *Lunar science conference, 5th, Houston, Tex., March 18-22, 1974, proceedings* (Vol. 1, pp. 887–906). Pergamon Press, Inc. Retrieved from <https://adsabs.harvard.edu/full/record/seri/LPSC/0005/1974LPSC....5..887M.html>
- Meyer, F., & Beucher, S. (1990). Morphological segmentation. *Journal of Visual Communication and Image Representation*, 1(1), 21–46. [https://doi.org/10.1016/1047-3203\(90\)90014-M](https://doi.org/10.1016/1047-3203(90)90014-M)
- Michikami, T., Kadokawa, T., Tsuchiyama, A., Hagermann, A., Nakano, T., Uesugi, K., & Hasegawa, S. (2018). Influence of petrographic textures on the shapes of impact experiment fine fragments measuring several tens of microns: Comparison with Itokawa regolith particles. *Icarus*, 302, 109–125. <https://doi.org/10.1016/j.icarus.2017.10.040>
- Morota, T., Haruyama, J., Ohtake, M., Matsunaga, T., Honda, C., Yokota, Y., et al. (2011). Timing and characteristics of the latest mare eruption on the Moon. *Earth and Planetary Science Letters*, 302(3), 255–266. <https://doi.org/10.1016/j.epsl.2010.12.028>
- Nie, J., Cui, Y., Senetakis, K., Guo, D., Wang, Y., Wang, G., et al. (2023). Predicting residual friction angle of lunar regolith based on Chang'e-5 lunar samples. *Science Bulletin*, 68(7), 730–739. <https://doi.org/10.1016/j.scib.2023.03.019>
- Otsu, N. (1979). A threshold selection method from gray-level histograms. *IEEE Transactions on Systems, Man, and Cybernetics*, 9(1), 62–66. <https://doi.org/10.1109/TSMC.1979.4310076>
- Perkins, S. W., & Madson, C. R. (1996). Mechanical and load-settlement characteristics of two lunar soil simulants. *Journal of Aerospace Engineering*, 9(1), 1–9. [https://doi.org/10.1061/\(ASCE\)0893-1321\(1996\)9:1\(1\)](https://doi.org/10.1061/(ASCE)0893-1321(1996)9:1(1))
- Qian, Y., She, Z., He, Q., Xiao, L., Wang, Z., Head, J. W., et al. (2023). Mineralogy and chronology of the young mare volcanism in the Procellarum-KREEP-Terrane. *Nature Astronomy*, 7(3), 287–297. <https://doi.org/10.1038/s41550-022-01862-1>
- Qian, Y., Xiao, L., Yin, S., Zhang, M., Zhao, S., Pang, Y., et al. (2020). The regolith properties of the Chang'e-5 landing region and the ground drilling experiments using lunar regolith simulants. *Icarus*, 337, 113508. <https://doi.org/10.1016/j.icarus.2019.113508>
- Qian, Y., Xiao, L., Zhao, J., Head, J. W., He, Q., Xu, H., et al. (2024). First magnetic and spectroscopic constraints on attenuated space weathering at the Chang'e-5 landing site. *Icarus*, 410, 115892. <https://doi.org/10.1016/j.icarus.2023.115892>
- Rousé, P. C., Fannin, R. J., & Shuttle, D. A. (2008). Influence of roundness on the void ratio and strength of uniform sand. *Géotechnique*, 58(3), 227–231. <https://doi.org/10.1680/geot.2008.58.3.227>
- Russ, J. C. (2013). *Fractal surfaces*. Springer Science & Business Media.
- Schmitt, H. H., Petro, N. E., Wells, R. A., Robinson, M. S., Weiss, B. P., & Mercer, C. M. (2017). Revisiting the field geology of taurus-littrow. *Icarus*, 298, 2–33. <https://doi.org/10.1016/j.icarus.2016.11.042>
- Shen, L., Farid, H., & McPeck, M. A. (2009). Modeling three-dimensional morphological structures using spherical harmonics. *Evolution*, 63(4), 1003–1016. <https://doi.org/10.1111/j.1558-5646.2008.00557.x>
- Shotton, J., Johnson, M., & Cipolla, R. (2008). Semantic texon forests for image categorization and segmentation. *2008 IEEE Conference on Computer Vision and Pattern Recognition*, 1–8. <https://doi.org/10.1109/CVPR.2008.4587503>

- Smith, M., Craig, D., Herrmann, N., Mahoney, E., Krezel, J., McIntyre, N., & Goodliff, K. (2020). The Artemis program: An overview of NASA's activities to return humans to the Moon. *2020 IEEE Aerospace Conference*, 1–10. <https://doi.org/10.1109/AERO47225.2020.9172323>
- Snape, J. F., Nemchin, A. A., Whitehouse, M. J., Merle, R. E., Hopkinson, T., & Anand, M. (2019). The timing of basaltic volcanism at the Apollo landing sites. *Geochimica et Cosmochimica Acta*, 266, 29–53. <https://doi.org/10.1016/j.gca.2019.07.042>
- Sommer, C., Straehle, C., Koethe, U., & Hamprecht, F. A. (2011). Ilastik: Interactive learning and segmentation toolkit. *2011 IEEE International Symposium on Biomedical Imaging: From Nano to Macro*, 230–233. <https://doi.org/10.1109/ISBI.2011.5872394>
- Steiglitz, R. D. (1988). Rock particles, fragments. In *General Geology* (pp. 711–716). Kluwer Academic Publishers. [https://doi.org/10.1007/0-387-30844-X\\_96](https://doi.org/10.1007/0-387-30844-X_96)
- Sudhyadhom, A. (2020). On the molecular relationship between Hounsfield Unit (HU), mass density, and electron density in computed tomography (CT). *PLoS One*, 15(12), e0244861. <https://doi.org/10.1371/journal.pone.0244861>
- Thompson, M. S., Zega, T. J., Becerra, P., Keane, J. T., & Byrne, S. (2016). The oxidation state of nanophase Fe particles in lunar soil: Implications for space weathering. *Meteoritics & Planetary Science*, 51(6), 1082–1095. <https://doi.org/10.1111/maps.12646>
- Tian, H.-C., Wang, H., Chen, Y., Yang, W., Zhou, Q., Zhang, C., et al. (2021). Non-KREEP origin for chang'e-5 basalts in the Procellarum KREEP Terrane. *Nature*, 600(7887), 59–63. <https://doi.org/10.1038/s41586-021-04119-5>
- Tomioka, N., & Fujino, K. (1997). Natural (Mg,Fe)SiO<sub>3</sub>-ilmenite and -perovskite in the Tenham meteorite. *Science*, 277(5329), 1084–1086. <https://doi.org/10.1126/science.277.5329.1084>
- Tsuchiyama, A., Sakurama, T., Nakano, T., Uesugi, K., Ohtake, M., Matsushima, T., et al. (2022). Three-dimensional shape distribution of lunar regolith particles collected by the Apollo and Luna programs. *Earth Planets and Space*, 74(1), 172. <https://doi.org/10.1186/s40623-022-01737-9>
- Watters, T. R., Weber, R. C., Collins, G. C., Howley, I. J., Schmerr, N. C., & Johnson, C. L. (2019). Shallow seismic activity and young thrust faults on the Moon. *Nature Geoscience*, 12(6), 411–417. <https://doi.org/10.1038/s41561-019-0362-2>
- Weber, I., Stojic, A. N., Morlok, A., Reitze, M. P., Markus, K., Hiesinger, H., et al. (2020). Space weathering by simulated micrometeorite bombardment on natural olivine and pyroxene: A coordinated IR and TEM study. *Earth and Planetary Science Letters*, 530, 115884. <https://doi.org/10.1016/j.epsl.2019.115884>
- Wei, D., Wang, J., Nie, J., & Zhou, B. (2018). Generation of realistic sand particles with fractal nature using an improved spherical harmonic analysis. *Computers and Geotechnics*, 104, 1–12. <https://doi.org/10.1016/j.compgeo.2018.08.002>
- Wei, D., Wang, J., & Zhao, B. (2018b). A simple method for particle shape generation with spherical harmonics. *Powder Technology*, 330, 284–291. <https://doi.org/10.1016/j.powtec.2018.02.006>
- Wieczorek, M. A. (2006). The constitution and structure of the lunar interior. *Reviews in Mineralogy and Geochemistry*, 60(1), 221–364. <https://doi.org/10.2138/rmg.2006.60.3>
- Wilkerson, R. P., Rickman, D. L., McElderry, J. R., Walker, S. R., & Cannon, K. M. (2024). On the measurement of shape: With applications to lunar regolith. *Icarus*, 412, 115963. <https://doi.org/10.1016/j.icarus.2024.115963>
- Woods-Robinson, R., Siegler, M. A., & Paige, D. A. (2019). A model for the thermophysical properties of lunar regolith at low temperatures. *Journal of Geophysical Research: Planets*, 124(7), 1989–2011. <https://doi.org/10.1029/2019JE005955>
- Wu, B., Huang, J., Li, Y., Wang, Y., & Peng, J. (2018). Rock abundance and crater density in the candidate Chang'e-5 landing region on the Moon. *Journal of Geophysical Research: Planets*, 123(12), 3256–3272. <https://doi.org/10.1029/2018JE005820>
- Wu, F.-Y., Li, Q.-L., Chen, Y., Hu, S., Yue, Z.-Y., Zhou, Q., et al. (2024). Lunar evolution in light of the Chang'e-5 returned samples. *Annual Review of Earth and Planetary Sciences*, 52(1), 159–194. <https://doi.org/10.1146/annurev-earth-040722-100453>
- Wu, H., Zou, Y., Zhang, C., Yang, W., Wu, B., Yung, K.-L., & Zhao, Q. (2025). Micro-CT Data of Chang'e 5 Lunar Regolith Particles [Dataset]. *Figshare*. <https://doi.org/10.6084/m9.figshare.27132516.v1>
- Xian, H., Zhu, J., Yang, Y., Li, S., Lin, X., Xi, J., et al. (2023). Ubiquitous and progressively increasing ferric iron content on the lunar surfaces revealed by the Chang'e-5 sample. *Nature Astronomy*, 7(3), 280–286. <https://doi.org/10.1038/s41550-022-01855-0>
- Xiao, Y., Yuan, Z., Chu, J., Liu, H., Huang, J., Luo, S. N., et al. (2019). Particle breakage and energy dissipation of carbonate sands under quasi-static and dynamic compression. *Acta Geotechnica*, 14(6), 1741–1755. <https://doi.org/10.1007/s11440-019-00790-1>
- Xie, H. (2020). *Fractals in rock mechanics*. CRC Press. <https://doi.org/10.1201/9781003077626>
- Yang, W., Chen, Y., Wang, H., Tian, H., Hui, H., Xiao, Z., et al. (2022). Geochemistry of impact glasses in the Chang'e-5 regolith: Constraints on impact melting and the petrogenesis of local basalt. *Geochimica et Cosmochimica Acta*, 335, 183–196. <https://doi.org/10.1016/j.gca.2022.08.030>
- Yang, Y., Jiang, T., Liu, Y., Xu, Y., Zhang, H., Tian, H.-C., et al. (2022). A micro mid-infrared spectroscopic study of Chang'e-5 sample. *Journal of Geophysical Research: Planets*, 127(8), e2022JE007453. <https://doi.org/10.1029/2022JE007453>
- Yao, Y., Xiao, C., Wang, P., Li, C., & Zhou, Q. (2022). Instrumental neutron activation analysis of Chang'e-5 lunar regolith samples. *Journal of the American Chemical Society*, 144(12), 5478–5484. <https://doi.org/10.1021/jacs.1c13604>
- Zhang, H., Zhang, X., Zhang, G., Dong, K., Deng, X., Gao, X., et al. (2021). Size, morphology, and composition of lunar samples returned by Chang'E-5 mission. *Science China Physics, Mechanics & Astronomy*, 65(2), 229511. <https://doi.org/10.1007/s11433-021-1818-1>
- Zhang, H., Zhang, X., Zhang, G., Dong, K., Deng, X., Gao, X., et al. (2022). Size, morphology, and composition of lunar samples returned by Chang'E-5 mission. *Science China Physics, Mechanics & Astronomy*, 65(2), 229511. <https://doi.org/10.1007/s11433-021-1818-1>
- Zhang, M., Fa, W., & Eke, V. R. (2023). Modeling the evolution of lunar regolith: 1. Formation mechanism through individual simple impact craters. *Journal of Geophysical Research: Planets*, 128(8), e2023JE007850. <https://doi.org/10.1029/2023JE007850>
- Zhao, B., & Wang, J. (2015). 3D quantitative shape analysis on form, roundness, and compactness with  $\mu$ CT. *Powder Technology*, 291, 262–275. <https://doi.org/10.1016/j.powtec.2015.12.029>
- Zhao, B., Wang, J., Andò, E., Viggiani, G., & Coop, M. R. (2020). Investigation of particle breakage under one-dimensional compression of sand using X-ray microtomography. *Canadian Geotechnical Journal*, 57(5), 754–762. <https://doi.org/10.1139/cgj-2018-0548>
- Zhou, B., Wang, J., & Zhao, B. (2015). Micromorphology characterization and reconstruction of sand particles using micro X-ray tomography and spherical harmonics. *Engineering Geology*, 184, 126–137. <https://doi.org/10.1016/j.enggeo.2014.11.009>
- Zhu, F., & Zhao, J. (2021). Interplays between particle shape and particle breakage in confined continuous crushing of granular media. *Powder Technology*, 378, 455–467. <https://doi.org/10.1016/j.powtec.2020.10.020>
- Zingg, T. (1935). *Beitrag zur schotteranalyse*. [PhD Thesis]. ETH Zurich.
- Zong, K., Wang, Z., Li, J., He, Q., Li, Y., Becker, H., et al. (2022). Bulk compositions of the Chang'E-5 lunar soil: Insights into chemical homogeneity, exotic addition, and origin of landing site basalts. *Geochimica et Cosmochimica Acta*, 335, 284–296. <https://doi.org/10.1016/j.gca.2022.06.037>